NeuroImage 244 (2021) 118605

Contents lists available at ScienceDirect

NeuroImage

journal homepage: www.elsevier.com/locate/neuroimage

Spatiotemporal characterisation of ischaemic lesions in transient stroke animal models using diffusion free water elimination and mapping MRI with echo time dependence

Ezequiel Farrher[a,1,*], Chia-Wen Chiang[b,1], Kuan-Hung Cho[b], Farida Grinberg[a], Richard P. Buschbeck[a], Ming-Jye Chen[b], Kuo-Jen Wu[c], Yun Wang[c], Sheng-Min Huang[b], Zaheer Abbas[a], Chang-Hoon Choi[a], N. Jon Shah[a,d,e,f], Li-Wei Kuo[b,g,**]

[a] Institute of Neuroscience and Medicine 4, INM–4, Forschungszentrum Jülich, Germany
[b] Institute of Biomedical Engineering and Nanomedicine, National Health Research Institutes, Miaoli, Taiwan
[c] Center for Neuropsychiatric Research, National Health Research Institutes, Miaoli, Taiwan
[d] Department of Neurology, RWTH Aachen University, Aachen, Germany
[e] JARA – BRAIN – Translational Medicine, Aachen, Germany
[f] Institute of Neuroscience and Medicine 11, INM–11, JARA, Forschungszentrum Jülich, Germany
[g] Institute of Medical Device and Imaging, National Taiwan University College of Medicine, Taipei, Taiwan

ARTICLE INFO

Keywords:
Diffusion tensor imaging
Free water elimination and mapping
Vasogenic oedema
Tissue cavitation
Transverse relaxation
Middle cerebral artery occlusion

ABSTRACT

Background and purpose: The excess fluid as a result of vasogenic oedema and the subsequent tissue cavitation obscure the microstructural characterisation of ischaemic tissue by conventional diffusion and relaxometry MRI. They lead to a pseudo-normalisation of the water diffusivity and transverse relaxation time maps in the subacute and chronic phases of stroke. Within the context of diffusion MRI, the free water elimination and mapping method (FWE) with echo time dependence has been proposed as a promising approach to measure the amount of free fluid in brain tissue robustly and to eliminate its biasing effect on other biomarkers. In this longitudinal study of transient middle cerebral artery occlusion (MCAo) in the rat brain, we investigated the use of FWE MRI with echo time dependence for the characterisation of the tissue microstructure and explored the potential of the free water fraction as a novel biomarker of ischaemic tissue condition.

Methods: Adult rats received a transient MCAo. Diffusion- and transverse relaxation-weighted MRI experiments were performed longitudinally, pre-occlusion and on days 1, 3, 4, 5, 6, 7 and 10 after MCAo on four rats. Histology was performed for non-stroke and 1, 3 and 10 days after MCAo on three different rats at each time point.

Results: The free water fraction was homogeneously increased in the ischaemic cortex one day after stroke. Between three and ten days after stroke, the core of the ischaemic tissue showed a progressive normalisation in the amount of free water, whereas the inner and outer border zones of the ischaemic cortex depicted a large, monotonous increase with time. The specific lesions in brain sections were verified by H&E and immunostaining. The tissue-specific diffusion and relaxometry MRI metrics in the ischaemic cortex were significantly different compared to their conventional counterpart.

Conclusions: Our results demonstrate that the free water fraction in FWE MRI with echo time dependence is a valuable biomarker, sensitive to the progressive degeneration in ischaemic tissue. We showed that part of the heterogeneity previously observed in conventional parameter maps can be accounted for by a heterogeneous distribution of free water in the tissue. Our results suggest that the temporal evolution of the free fluid fraction map at the core and inner border zone can be associated with the pathological changes linked to the evolution

Abbreviations: FWE, free water elimination; MCAo, middle cerebral artery occlusion; DW, diffusion-weighted; ADC, apparent diffusion coefficient; PVE, partial volume effect; $FWET_2$, free water elimination with explicit T_2 attenuation; DTI, diffusion tensor imaging; T_2W, T_2-weighted; $DTIT_2$, diffusion tensor imaging with explicit T_2 attenuation; FA, fractional anisotropy; MD, mean diffusivity; AIC, Akaike information criterion; SEM, standard error of the mean; std, standard deviation; CRLB, Cramr-Rao lower bound.

* Corresponding author.
** Corresponding author at: Institute of Biomedical Engineering and Nanomedicine, National Health Research Institutes, Miaoli, Taiwan.
E-mail addresses: e.farrher@fz-juelich.de (E. Farrher), lwkuo@nhri.edu.tw (L.-W. Kuo).
[1] These authors have contributed equally to this work.

https://doi.org/10.1016/j.neuroimage.2021.118605.
Received 10 November 2020; Received in revised form 14 September 2021; Accepted 19 September 2021
Available online 28 September 2021.

of vasogenic oedema. Namely, the homogeneous increase in free water one day after stroke and its tendency to normalise in the core of the ischaemic cortex starting three days after stroke, followed by a progressive increase in free water at the inner border zone from three to ten days after stroke. Finally, the monotonous increase in free fluid in the outer border zone of the cortex reflects the formation of fluid-filled cysts.

1. Introduction

MRI is a powerful tool for the characterisation of ischaemic tissue in all phases of stroke, both for humans and animal models (Hoehn et al., 2001; Sotak, 2002; Weber et al., 2006). As one of the major MRI contrast mechanisms, diffusion-weighted (DW) MRI is unique in that it enables localisation of the ischaemic region within the first half an hour after the stroke onset (Sotak, 2002). Indeed during the hyperacute (< 2 h post stroke) and acute (2–3 h) phases of stroke, the apparent diffusion coefficient (ADC) is strongly reduced (Moseley et al., 1990; Sotak, 2002), whereas some of the so-called non-Gaussian diffusion biomarkers, e.g. the mean kurtosis, show increased values (Grinberg et al., 2014, 2012; Hui et al., 2012; Jensen et al., 2011). These alterations have generally been associated with inter-compartmental water shift and cell swelling as a result of cytotoxic oedema (Knight et al., 1991), changes in membrane permeability (Lätt et al., 2009) and the amount of bound water (Bihan, 2007), the degradation of intracellular organelles (Van Pul et al., 2005), and neurite beading (Budde and Frank, 2010). Conversely, the transverse relaxation time (T_2) is unaffected during the hyperacute phase and only begins to change during the acute phase (Carano et al., 2000; Helpern et al., 1993; Knight et al., 1994; Ordidge et al., 1991). Proposed mechanisms for the early rise in conventional T_2 values include the increase in the total water content (Kamman et al., 1988; Knight et al., 1991; T. N. Lin et al., 2002; Matsumoto et al., 1995), the breakdown of cellular structures and the increase in non-bound water (Ordidge et al., 1991). In the subacute phase of stroke (≥ 1 day), both DW and T_2-relaxometry MRI parameters are further affected by the development of vasogenic oedema and the subsequent disruption of the cytoarchitecture (Carano et al., 2000). In the days following stroke, DW and T_2-relaxometry metrics start renormalising, with an increase in the ADC (Carano et al., 2000; Knight et al., 1991; Pierpaoli et al., 1993) and a decrease in the non-Gaussian metrics (Hui et al., 2012) and T_2 values (Carano et al., 2000; Knight et al., 1991; S. P. Lin et al., 2002; Wagner et al., 2012). This renormalisation process is highly heterogeneous with region-dependent normalisation rates, which has been attributed to the resolution of vasogenic oedema (S. P. Lin et al., 2002; Wagner et al., 2012). Finally, in the late subacute and chronic phases (≥ 7 days), further degradation of cell membranes, tissue cavitation and formation of fluid-filled cysts result in a secondary increase in the ADC and T_2 and a further reduction in non-Gaussian metrics (Helpern et al., 1993; Hui et al., 2012; Jiang et al., 1997, 1993; Knight et al., 1994; Wegener et al., 2006).

DW and T_2-relaxometry MRI metrics can only be considered tissue-specific if the voxel contains a single type of tissue. If the voxel is affected by the partial volume effect (PVE), the metric integrates the effect of all tissue types in the voxel. In particular, the PVE with cerebrospinal fluid (CSF) can greatly affect DW and relaxometry parameters given that CSF is characterised by diffusion coefficient and T_2 values several times larger than those values for tissue (Alexander et al., 2001; Piechnik et al., 2009).

Within the framework of DW MRI, Pierpaoli and Jones (2004) reported that both vasogenic oedema and CSF have similar diffusion properties and therefore affect the DW MRI signal in a similar manner. They proposed the use of a two-compartment model, with one of the compartments referring to free fluid (free, isotropic diffusion) and the other to tissue (restricted, anisotropic diffusion). However, the parameter estimation problem for this model is generally challenging (Bergmann et al., 2020; Hoy et al., 2014) and, for single-shell diffusion encoding schemes, even ill-posed (Pasternak et al., 2009). Mitigations to these problems include the acquisition of several diffusion weightings (b-values) (Pierpaoli and Jones, 2004), the addition of a spatial regularisation of the tissue diffusion tensor (Pasternak et al., 2009), and constraints in the fitting parameters (Arkesteijn et al., 2017). Recently, it has been demonstrated that, due to the difference in T_2 of free water and tissue, the explicit modelling of the T_2-attenuation for each compartment, together with the acquisition of different T_E values, leads to a more accurate, precise and robust estimation of the model parameters (Collier et al., 2017; Farrher et al., 2020; Molina-Romero et al., 2018). The underlying idea of this approach is inspired by the well-known multidimensional NMR methods (Bernin and Topgaard, 2013; van Dusschoten, 1996, 1995). However, there is a fundamental difference between the aforementioned multidimensional NMR methods, which are based on the inversion of the Laplace transform, and the FWE model with explicit account of T_2 attenuation ($FWET_2$), in which the number of physical compartments is defined *a priori*. Furthermore, the difference in T_2 of the tissue and water compartments leads to a T_E dependence of the relative free water fraction if that difference is not explicitly modelled (Collier et al., 2017; Pasternak et al., 2009). FWE DTI affords several benefits, the most notable being the reduction in the bias in DTI metrics and fibre tractography (Arkesteijn et al., 2017; Hoy et al., 2015; Metzler-Baddeley et al., 2012), and the improvement of the test-retest reproducibility (Albi et al., 2017). Moreover, the free water fraction map has been shown to be a sensitive biomarker for vasogenic oedema in tumours (Pasternak et al., 2009) and neurodegenerative diseases such as dementia (Maier-Hein et al., 2015), Alzheimer's disease (Hoy et al., 2017) and Parkinson's disease (Ofori et al., 2015; Planetta et al., 2016).

The aim of this work is to demonstrate the use of $FWET_2$ for the characterisation of the spatiotemporal evolution of ischaemia after transient middle cerebral artery occlusion (MCAo) stroke in rats. In the first part, we performed a quantitative validation of the $FWET_2$ approach, compared to conventional DTI and T_2-relaxometry, for modelling the DW and T_2W MRI signal in the rat brain tissue. In the second part, we characterised the spatiotemporal evolution of ischaemia after stroke by means of $FWET_2$. In particular, we assessed the potential of the free water fraction (provided by $FWET_2$) as a novel biomarker of neuropathological changes in ischaemia. We also compared the tissue-specific diffusion and transverse relaxation time provided by $FWET_2$ with those attained using conventional DTI and monoexponential T_2-relaxometry methods. That is to say, we evaluated the extent to which the features shown by conventional DTI and T_2-relaxometry methods can be accounted for by the presence of a free water compartment within the voxel of interest. Finally, we related the $FWET_2$ maps with histopathology scores and discussed the findings in light of the biophysical mechanisms examined in the literature.

2. Materials and methods

2.1. $FWET_2$ model

The $FWET_2$ model assumes that the DW and T_2W MRI signal originates from two compartments with different transverse relaxation times and diffusion properties, in the slow-exchange regime (Collier et al., 2017; Pasternak et al., 2009). The signal is written as follows

$$S(T_E, b, \mathbf{n}) = S_0 \left[f_w e^{-\frac{T_E}{T_{2,w}}} e^{-bD_w} + (1 - f_w) e^{-\frac{T_E}{T_{2,t}}} e^{-b\mathbf{n}^T \mathbf{D}_t \mathbf{n}} \right], \quad (1)$$

where S_0 is the proton density, D_w and $\mathbf{D}_t$ are the diffusion coefficient and tensor for the free water and tissue compartments, respectively, $T_{2,w}$ and $T_{2,t}$ denote the transverse relaxation times for the free water and tissue compartments, respectively, and f_w is the T_E-independent free water fraction. The experimentally controlled parameters are the strength and direction of the diffusion weighting, b and $\mathbf{n} = (n_x, n_y, n_z)^T$, respectively, and the echo time T_E. Note that an additional multiplicative term of the form $(1 - e^{-T_R/T_{1,c}})$ for each compartment in Eq. (1) should be included *a priori* ($c = w,\ t$). However, this term can be neglected if the repetition time fulfils the condition $T_R \gg T_{1,c}$.

Assuming a voxel containing a single tissue type, the simplest representation of the DW and T_2W MRI signal is written as follows:

$$S\left(T_E, b, \mathbf{n}\right) = S_0 e^{-\frac{T_E}{T_2}} e^{-b\mathbf{n}^T\mathbf{D}\mathbf{n}}, \tag{2}$$

where T_2 and $\mathbf{D}$ are the transverse relaxation time and diffusion tensor, respectively (Pierpaoli and Basser, 1996). Eq. (2) merely represents the DTI signal with an explicit T_2 exponential attenuation ($DTIT_2$).

2.2. Animal model

All procedures and experiments were approved by the Institutional Animal Care and Use Committee at the National Health Research Institutes (Taiwan). Adult male Sprague-Dawley rats (BioLASCO, Taipei, Taiwan), weighing 300–400 g, were anesthetised with chloral hydrate (0.4 g/kg, intraperitoneal injection; Sigma-Aldrich). The right middle cerebral artery (MCA) was ligated with a 10–0 suture (N-2540, Monosof™ Covidien, Minneapolis, MN, USA) and common carotid arteries were clamped bilaterally using non-traumatic arterial clips, together efficiently reducing > 80% blood flow in the MCA, causing consistently focal ischaemia in the cerebral cortex, as described previously (Chen et al., 1986; Liu et al., 2011; Yu et al., 2020). The ligature and clamps were removed after 90 min to generate reperfusion injury. Core body temperature was monitored and maintained at 37 °C by a heating pad during surgery. After recovery from the anaesthesia, the body temperature was maintained at 37 °C using a temperature-controlled incubator.

The animals were assigned to two groups. The first group contained four rats subjected to a longitudinal MRI assessment, including assessment prior to stroke (pre-occlusion) and on days 1, 3, 4, 5, 6, 7 and 10 after MCAo. The second group contained twelve rats sacrificed immediately after individual MRI scan. Four time points were defined, namely non-stroke, and 1, 3, and 10 days after MCAo (three rats for each time point). A custom-made rat head holder and a circulating heated water bath were used. All rats were anesthetised with 1–2% isoflurane in oxygen during the MRI scans. Respiration was kept at 40–50 breaths per minute, and body temperature was maintained at 37 °C. This was monitored using a small animal physiological monitoring and control unit (SA Instruments, Stony Brook, NY).

2.3. MRI experiments

Experiments were performed on a home-integrated, translational 3T MRI scanner equipped with an ultra-high-strength gradient coil (maximum strength of 675 mT/m) (Cho et al., 2019). A custom-built, single-loop transmit/receive surface coil was utilised. A Stejskal-Tanner segmented echo-planar imaging (EPI) pulse sequence (EVO, MR Solutions Ltd., UK) was used. The acquisition parameters were: repetition-time, T_R = 9 s; echo-time, T_E = 50, 100 ms; b-values (directions) = 0 (8), 0.5 (12) and 1.0 (26) and 2.0 (40) ms/μm^2 (b = 2.0 ms/μm^2 was not used in this work); diffusion gradient separation and duration, Δ = 24 ms and δ = 3 ms; one repetition. Additionally, eight b = 0 images (eight repetitions) with T_E = 70, 90, 110, 130 ms were acquired. Other parameters were: field-of-view, FOV = 25 × 25 mm^2; matrix-size = 96 × 96; voxel-size = 0.26 × 0.26 × 1 mm^3; 20 image slices; phase-encoding direction AP. One extra volume with opposite phase encoding was acquired for the correction of distortions induced by tissue susceptibility differences. A turbo spin-echo sequence was used to acquire T_2-weighted structural images. The protocol parameters were: T_R = 4 s; T_E = 68 ms; six repetitions; FOV = 25 × 25 mm^2; matrix-size = 192 × 192; voxel-size = 0.13 × 0.13 × 1 mm^3; 20 image slices. The scan time for the DW and T_2W data acquisition was approximately 1 h and 20 min per rat.

2.4. Model parameter estimation

The data processing pipeline is similar to Farrher et al. (2020). Prior to the estimation of model parameters, the data were denoised using the adaptive optimised nonlocal means method (Manjón et al., 2010). Susceptibility-induced and eddy-current distortions were corrected using `topup` and `eddy`, provided by FSL (Andersson et al., 2003; Smith et al., 2004). Gibbs-ringing artefact correction was performed using the total variation approach implemented in the toolkit ExploreDTI (Leemans et al., 2009; Perrone et al., 2015). Similarly to Veraart et al. (2017), correction of the positive signal bias due to its Rician nature was performed following the method described by Gudbjartsson and Patz (1995), with the estimation of the background noise standard deviation, σ, using the approach proposed by Aja-Fernández et al. (2009). The remaining processing was completed using in-house Matlab scripts (Matlab 2015a, The MathWorks, MA, USA). $FWET_2$ model (Eq. (1)) parameter estimation was performed in two steps:

(i) $DTIT_2$ model parameters were estimated by fitting Eq. (2) to the experimental dataset (DW and T_2W, Fig. 1a), in order to generate an initial guess for $T_{2,t}$ and $\mathbf{D}_t$. Estimation was performed via weighted-linear least-squares, which for the $DTIT_2$ model parameters, $\theta_{DTIT_2} = [\ln S_0, D_{xx}, D_{xy}, D_{xz}, D_{yy}, D_{yz}, D_{zz}, 1/T_2]^T$, is written as follows:

$$\hat{\theta}_{DTIT_2} = \left(\mathbf{X}^T\mathbf{w}\mathbf{X}\right)^{-1}\mathbf{X}^T\mathbf{w}\mathbf{y}, \tag{3}$$

where $\mathbf{y}$ ($N \times 1$) is a column vector whose elements are given by the natural logarithm of the N measured signals, i.e. $y_i = \ln M_i$ ($i = 1 \ldots N$) and the weighting matrix, $\mathbf{w}$ ($N \times N$), is a diagonal matrix whose elements are given by $w_{i,i} = M_i^2$. The i^{th} row of the design matrix, $\mathbf{X}$ ($N \times 8$), is written as $X_{i,:} = [1, -b_i n_{ix}^2, -2b_i n_{ix}n_{iy}, -2b_i n_{ix}n_{iz}, -b_i n_{iy}^2, -2b_i n_{iy}n_{iz}, -b_i n_{iz}^2, -T_{E,i}]$.

(ii) $FWET_2$ model parameters, $\theta_{FWET_2} = [S_0, f_w, D_{xx}, D_{xy}, D_{xz}, D_{yy}, D_{yz}, D_{zz}, T_{2,t}]^T$, were estimated via constrained non-linear minimisation of the least-squares estimator, which is written as

$$\hat{\theta}_{FWET_2} = \arg\min_{\theta_{FWET_2}} \|\mathbf{M} - \mathbf{S}\left(T_{E,i}, b_i, \mathbf{n}_i; \theta_{FWET_2}\right)\|^2, \tag{4}$$

where the elements of the vector $\mathbf{S}(T_{E,i}, b_i, \mathbf{n}_i; \theta_{FWET_2})$ are given by the signal model (Eq. (1)) evaluated at $(T_{E,i}, b_i, \mathbf{n}_i)$. Minimisation of Eq. (4) was performed with the help of the function `fmincon` available in Matlab using the `interior-point` algorithm. T_2 and $\mathbf{D}$ estimated in step (i) were used as initial guess for $T_{2,t}$ and $\mathbf{D}_t$, with an exhaustive solution search in the parameters space along the f_w dimension. The following linear and non-linear constraints were imposed:

(a) Linear constraints: $0 \le f_w \le 1$

(b) Non-linear constraints: $0 \le \lambda_k \le 1.1 D_w$ ($k = 1, 2, 3$), where λ_k denotes the eigenvalues of the tissue diffusion tensor $\mathbf{D}_t$ ($\lambda_1 \ge \lambda_2 \ge \lambda_3$) (Grinberg et al., 2011a).

Free water parameters were fixed to $T_{2,w}$ = 502 ms (Piechnik et al., 2009) and D_w = 3 μm^2/ms (Alexander et al., 2001).

Due to the long longitudinal relaxation time of CSF ($T_{1,w}$ = 4.3 s) (Abbas et al., 2014) compared to T_R, we included a multiplicative term equal to $(1 - e^{-T_R/T_{1,w}}) \approx 0.88$ in the free water compartment in order to account for incomplete signal recovery. For the tissue compartment, the condition $T_R \gg T_{1,t}$ holds. DTI parameters FA and MD were evaluated as described elsewhere (Basser and Pierpaoli, 1996). Here they are denoted as FA and MD for the case of $DTIT_2$ and FA_t and MD_t (tissue-specific) for $FWET_2$. The signal-to-noise ratio (SNR) values were further calculated as SNR = S_0/σ.

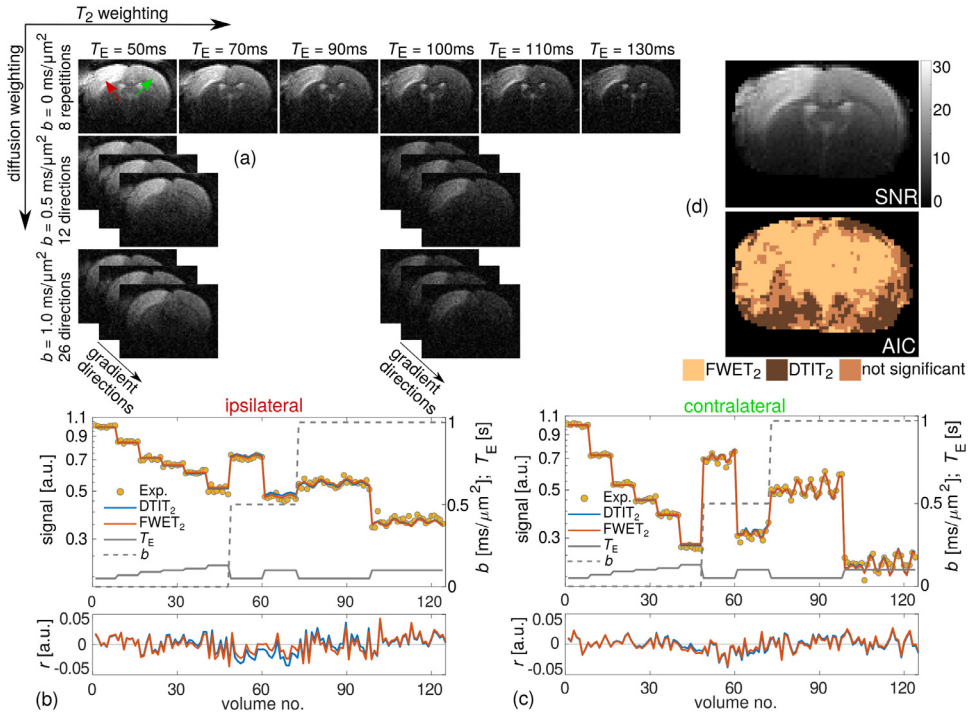

Fig. 1. (a) Schematic representation of the experimental setup. (b,c-top) Signal attenuation due to transverse relaxation and diffusion, shown as a function of the volume number along with the related model fit ($DTIT_2$, blue line; $FWET_2$, red line), for one voxel selected from the ipsilateral side and one voxel from the contralateral one (red and green arrows, respectively, in the top-left image). The corresponding b-value (grey, dashed lines) and T_E value (grey, solid lines) are also shown. (b,c-bottom) Plots of the residuals for $FWET_2$ (red lines) and for $DTIT_2$ (blue lines). (d-top) A map of the SNR. (d-bottom) A map of the threshold difference between the AIC values for both models: light-brown, $FWET_2$ statistically better than $DTIT_2$; dark-brown, $DTIT_2$ statistically better than $FWET_2$. All images and maps refer to slice 2 (Bregma −0.48 mm) (Paxinos and Watson, 2004).

2.5. Model validation

First, a comparison of the goodness-of-fit of the signal models $DTIT_2$ and $FWET_2$ was performed by plotting the residuals of the fit for all experimental data points, defined as $r_i = M_i - S(T_{E,i}, b_i, \mathbf{n}_i; \boldsymbol{\theta})$, $(i = 1 \dots N)$. Secondly, we used the corrected Akaike information criterion (AIC) (Burnham and Anderson, 1998; Veraart et al., 2017) to decide whether a better model fit is the result of an excess of degrees of freedom or due to a higher probability that one of the models describes the experimental data better than the other. The corrected AIC is defined as $AIC = 2k + N\ln(\|\mathbf{r}\|^2) + 2k(k+1)/(N-k-1)$, where $\mathbf{r}$ is the vector of residuals and k is the number of degrees of freedom, i.e. $k = 8$ for $DTIT_2$ and $k = 9$ for $FWET_2$. A difference in AIC values between models greater or equal to 2 is considered to be statistically significant (Burnham and Anderson, 1998).

2.6. Statistical analysis of $FWET_2$ and $DTIT_2$ parameters

The regions-of-interest (ROIs) on the ipsilateral and contralateral sides were manually drawn on slices 1 and 2 (Bregma 0.48 mm and −0.48 mm, respectively (Paxinos and Watson, 2004)) so as to cover the cortex, using the colour-coded FA maps as a guide (inset in Fig. 4a). Note that, due to the limited spatial resolution of our data, analysis of the external capsule was not conducted.

The mean and standard deviation of all parameters were calculated for each animal and each time point separately for all voxels in the entire ROIs in slices 1 and 2. We denote the mean and standard deviation of a parameter A over a given ROI as $\bar{A}$ and σ_A, respectively. Furthermore, the mean, $\langle \bar{A} \rangle$, and the standard error of the mean (SEM) over animals were computed and plotted against the time after occlusion. In order to investigate the temporal evolution of the biologically-induced ROI heterogeneity for each parameter (Wagner et al., 2012), the coefficient of variation of each parameter over the ROIs, defined as $\mathrm{CoV}_A = \sigma_A / \bar{A}$, was evaluated for each animal. Thereafter, the mean, $\langle \mathrm{CoV}_A \rangle$, and the corresponding SEM were computed over the animals and plotted as a function of time after occlusion.

The goal of the statistical analysis was two-fold. Firstly, we aimed to test for significant differences between the ipsilateral and contralateral ROIs for each time point and each $FWET_2$ parameter using a two-tailed paired t-test. Secondly, we aimed to compare $DTIT_2$ versus $FWET_2$ parameters in the ipsilateral ROI, also using a two-tailed paired t-test.

2.7. Group-based template analysis

In order to evaluate the spatial heterogeneity of f_w across animals in a voxel-wise manner, a group-based template was created for each time point. This was achieved using the FA from $DTIT_2$ via 2-dimensional, linear and non-linear registration with the help of the scrip `antsMultivariateTemplateConstruction2.sh`, available in ANTs (Avants et al., 2011). Subsequently, the affine transformation (firstly) and the warp field (secondly) were applied to f_w maps of each animal. Finally, a voxel-wise mean, $\langle f_w \rangle$, and standard deviation, std, of the f_w maps over the four animals were calculated for each time point.

2.8. Histology

A total of twelve animals were used for hematoxylin and eosin (H&E) stain and immunohistochemistry (IHC). The animals were sacrificed immediately after individual MRI. The animals were deeply anesthetised and transcardially perfused with 0.9% saline, followed by 4% paraformaldehyde (PFA, Sigma-Aldrich) in a 0.1 M phosphate buffer (PB, Sigma-Aldrich), pH 7.3. Brains were dissected from the skull and post-fixed for 24 h at 4 °C in PFA solution. Coronal paraffin-embedded brain sections were sliced at 4 μm thick and collected close to the Bregma −0.48 mm.

For H&E staining, an automated slide staining system (Tissue-Tek DRS 2000, Sakura Finetek Europe, Netherlands) was used, and the standard protocol of the manufacturer was followed. For IHC, tissue sections adjacent to those processed by H&E were incubated with the primary antibody: polyclonal rabbit anti-ionised calcium-binding adaptor molecule 1 (Iba-1, 1:100, GTX10042, GeneTex) or anti-glial fibrillary acidic protein antibody (GFAP, 1:1000, ab7260, Abcam). The detection was processed in the Discovery XT automated IHC/ISH slide staining system (Ventana Medical Systems, Inc., Tucson, US), using the ultraView Universal DAB Detection Kit (Ventana Medical Systems, Inc.,

Tucson, US), according to the manufacturer's instructions. The reaction product on the tissue section was visualised by the chromogen 3,3′-diaminobenzidine (DAB, brown). Counterstaining with hematoxylin (purple) was then additionally performed. A negative control without the primary antibody was prepared to evaluate the specificity of IHC test.

All stained brain sections were imaged with Pannoramic MIDI (3DHISTECH, Ltd., Hungary), a digital pathology slide scanning system (Objective: Plan-Apochromat 20×; Camera: CIS VCC-FC60FR19CL, 1.6×; micrometer/pixel: 0.243094) and CaseViewer software (3DHISTECH, Ltd., Hungary). In this study, the H&E images were evaluated by scoring the injury severity of the histopathological features, while the images of Iba-1 and GFAP staining were assessed qualitatively and subjectively for immunoreactivity changes without computer-assisted image analysis.

2.9. Histopathological analysis

All H&E stains were analysed for tissue pathology at the lesion by injury scoring. The lesioned cortex was divided into three sub-regions from the outside inwards: outer border zone, core area, and inner border zone. This was done by dividing line segments in the ratio of 1:3:1, perpendicular to the cortical surface and the external capsule (Fig. 8a). A 3-point scoring system was used to evaluate the injury severity (0 = no pathological injury; 1 = mild injury; 2 = moderate injury; 3 = severe injury). To evaluate the neuropathological tissue changes, we examined four to six images, evenly distributed in the individual sub-regions of the lesion, the aim being to comprehensively sample the whole lesioned cortex. The images were captured using a 20× objective lens. For each histopathological feature, the severity score was calculated as the mean of the scores obtained from the four or six representative images in each sub-region of the brain. Histopathological features of interest were assessed and scored, including (1) cerebral subleptomeningeal oedema, defined as enhanced space containing CSF; (2) liquefactive necrosis, resulting in disruption of the tissue cytoarchitecture and the formation of fluid-filled cysts; (3) perivascular oedema, characterised by vasogenic oedema; (4) vacuolation of neuronal cell, defined as acute cell injury; (5) vacuolation of the neuropil, defined as spongiosis and oedema and (6) cavitation, including cavitative lesions and cyst-like cavities. Analysis was performed in a blind manner by two examiners. The severity score was then determined as the average of the scores obtained by both examiners. We aimed to examine the injury severity of histopathological features on different sub-regions in relation to stroke time course. In addition, the corresponding $\langle \overline{f_w} \rangle$ values were evaluated in the same animal in order to investigate the correspondence of f_w with the histopathological features.

2.10. Data and code availability statement

Experimental data published in this work and scripts will be available via formal request to the corresponding authors and a signed data-sharing agreement.

3. Results

3.1. Model validation

A scheme of the experimental design is shown in Fig. 1a, demonstrating the signal attenuation due to both transverse relaxation and diffusion. The plots in Fig. 1b,c (top) show the signal attenuation versus acquisition volume number along with the related model fit for one voxel selected from the ipsilateral side and one from the contralateral side (red and green arrows, respectively, in Fig. 1a). The corresponding b-value (grey, dashed lines) and T_E value (grey, solid lines) are also shown in order to demonstrate each experimental parameter. The plots of the residuals shown in Fig. 1b (bottom) demonstrate that for b-value = 0.5 ms/μm^2, the residuals for $FWET_2$ (red lines) tend to be closer to zero than those for $DTIT_2$ (blue lines), especially in the ipsilateral voxel. The map of the threshold difference between the AIC values (Veraart et al., 2017) for both models (Fig. 1d, bottom) demonstrates that $FWET_2$ provides a statistically better fitting of the experimental data than $DTIT_2$ in the majority of the voxels. Some exceptions in the bottom of the brain are observed where the SNR values fall below ~5 (see the SNR map in Fig. 1d, top).

3.2. Spatiotemporal evolution of $DTIT_2$ vs $FWET_2$ parameters

An overview of the spatiotemporal evolution of the $FWET_2$ maps for slice 2 (Bregma −0.48 mm) for a representative animal is summarised in Fig. 2, alongside the $DTIT_2$ maps and the high-resolution, T_2-weighted images. MD and MD_t were both homogeneously reduced in the cortex on day 1. Between days 3 and 7, MD and MD_t tended to renormalise at the core of the affected area, whereas there was an increase of MD and MD_t above normal values at the inner border zone between the external capsule and the cortex (red arrows). In this border zone, the values reached a peak on day 4, dropped towards day 7 and rose again on day 10. Moreover, MD appeared brighter than MD_t. A later, steady increase both in MD and MD_t, starting five days after stroke (white arrows), was observed in the outer border zone.

Both FA and FA_t were homogeneously reduced in the whole cortex between days 1 and 10. Besides the well-known reduction of the conventional FA in the ipsilateral cortex (Carano et al., 2000), other changes were not observed in either FA or FA_t during the whole time period.

An increase in both T_2 and $T_{2,t}$ in the cortex was observed on day 1. Between days 3 and 7, T_2 and $T_{2,t}$ tended to normalise at the core area, with T_2 being much more heterogeneous than $T_{2,t}$ (black arrows). Moreover, T_2 at the inner border zone remained high and peaked at 4 days after stroke, whereas the normalisation of $T_{2,t}$ was much slower compared to that of T_2. By day 10, both T_2 and $T_{2,t}$ had similar values at the core, yet larger values compared to the contralateral side. At the outer border zone, T_2 appeared to steadily increase, whereas $T_{2,t}$ remained constant and comparable to the lesion core (white arrows).

Before occlusion, f_w at the external capsule and the corpus callosum showed slightly higher values compared to the cortex. Voxels around the ventricles that were affected by PVE with CSF showed the typical pattern of higher values compared to tissue-only voxels (Pasternak et al., 2009). Note that the estimation of f_w seems much more unstable in the lower part of the brain due to the low SNR values in that region (Fig. 1d, top) (Hoy et al., 2014). One day after stroke, f_w homogeneously increased in the whole cortex and external capsule. Between days 3 and 7, f_w in the ischaemic core tended to slowly normalise in a heterogeneous manner. An example of this can be seen in the areas depicted by the magenta arrows in Fig. 2d, which normalise at different rates. In addition, increasing f_w values can be seen in the inner border zone, with the peak occurring on day 4 after stroke (green arrow). Between days 5 and 7, f_w decreased slightly and then rose again on day 10. In contrast, at the outer border zone, f_w started increasing in a steady manner after 4 days (white arrows).

Fig. 3a–d illustrates the histograms of $FWET_2$ parameters f_w, MD_t, FA_t and $T_{2,t}$ taken over the ipsilateral and contralateral hemispheres for slices 1 and 2. Four representative time points are depicted as examples. The corresponding scatter plots of MD_t, FA_t and $T_{2,t}$ versus f_w are also shown. All histograms for the contralateral hemisphere and all parameters have a unimodal distribution. Conversely, all histograms for the ipsilateral hemisphere show a double modal distribution 1 day after stroke. A shift towards higher values for f_w and $T_{2,t}$ for the peak related to the affected area was observed, whereas for MD_t and FA_t the shift happened towards the lower values. Between days 4 and 10, the bimodal distribution holds for FA_t and $T_{2,t}$, whereas MD_t tends to show a unimodal distribution with the peak for the affected area becoming a shoulder-like shape as a consequence of the renormalisation. During this

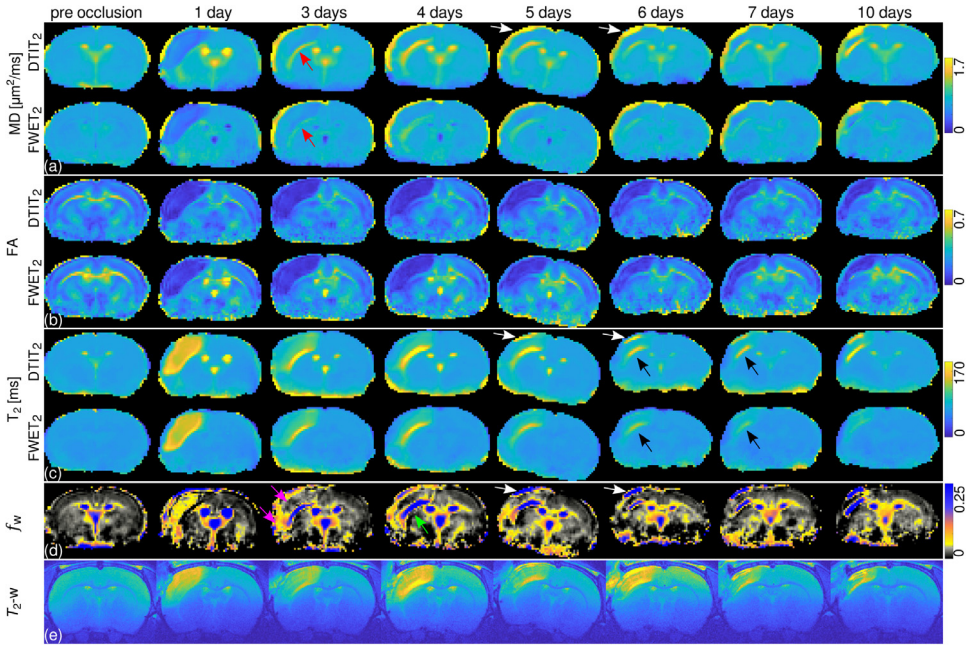

Fig. 2. Spatiotemporal evolution of the maps of MD and MD_t (a), FA and FA_t (b), T_2 and $T_{2,t}$ (c), f_w (d) and high-resolution, T_2-weighted images (e). All maps are shown for slice 2 (Bregma −0.48 mm) (Paxinos and Watson, 2004). Note that the colour scale of f_w is not linear, and the grey colours indicate normal healthy tissue values ($f_w \sim< 0.05$).

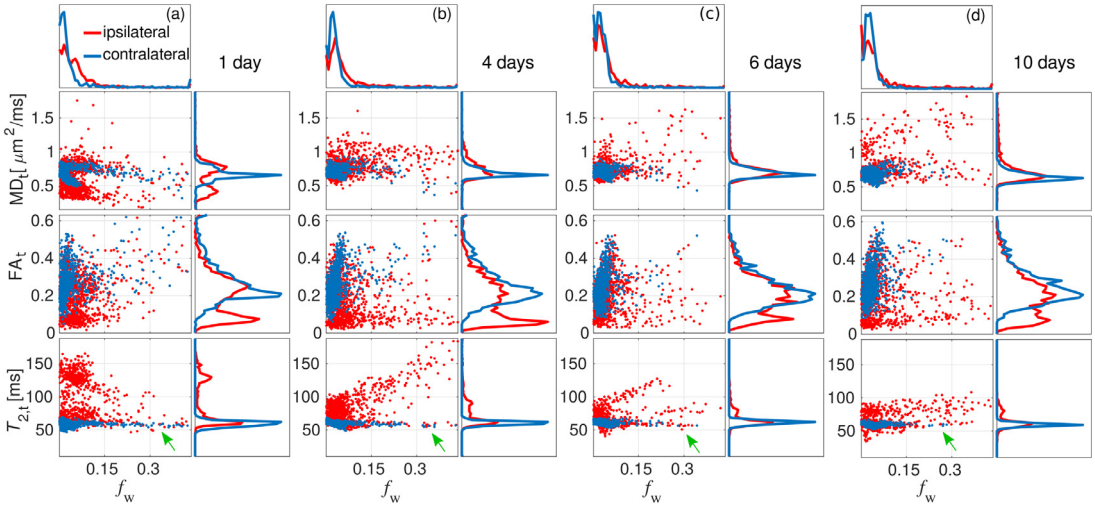

Fig. 3. Histograms of f_w, MD_t, FA_t and $T_{2,t}$ taken over the contralateral (blue) and ipsilateral (red) hemispheres, for slices 1 and 2 (Bregma 0.48 mm and −0.48 mm, respectively) (Paxinos and Watson, 2004) and 4 representative time points: 1 day (a), 4 days (b), 6 days (c) and 10 days (d) after stroke. The corresponding scatter plots of MD_t, FA_t and $T_{2,t}$ versus f_w are additionally shown. Green arrows refer to the tail of points coming from the ventricles and the voxels at the tissue-CSF interface.

Table 1
Spearman's correlation coefficient for MD_t, FA_t, and $T_{2,t}$ vs. f_w. The analysis was performed for the contralateral (ctrl) and the ipsilateral (ipsi) hemispheres as well as for the ipsilateral hemisphere with the constraint $f_w \geq 0.07$, i.e. abnormal f_w points (ipsi abn). Note that voxels at the ventricles and at the interface between tissue and CSF (green arrows in Fig. 3) were masked out for the correlation analysis. *, $p < 0.05$; **, $p < 0.005$.

	MD_t vs. f_w			FA_t vs. f_w			$T_{2,t}$ vs. f_w		
day	ctrl	ipsi	ipsi abn	ctrl	ipsi	ipsi abn	ctrl	ipsi	ipsi abn
1	−0.34**	−0.22**	−0.19**	0.43**	−0.19**	0.10	−0.38**	0.21**	−0.36**
4	−0.14**	0.28**	0.22**	0.45**	−0.20**	−0.08	−0.57**	0.28**	0.79**
6	−0.42**	0.07 *	0.66**	0.46**	0.15**	−0.28*	−0.56**	−0.14**	0.32**
10	−0.31**	0.05	0.03	0.51**	0.10**	0.18*	−0.64**	0.12*	0.48**

time, f_w also shows a unimodal distribution, with an increasing number of abnormally high values.

The scatter plots for MD_t, FA_t and $T_{2,t}$ versus f_w in Fig. 3 demonstrate distinctive features between the contralateral and the ipsilateral hemispheres. The Spearman's correlation coefficients for each hemisphere are listed in Table 1. Coefficients for all three pairs of parameters for the contralateral hemispheres show the same consistent trend for all time points. The behaviour for the ipsilateral hemisphere is more complex, with the sign of the correlation being dependent on the time point. A correlation analysis restricted to voxels showing relatively high free

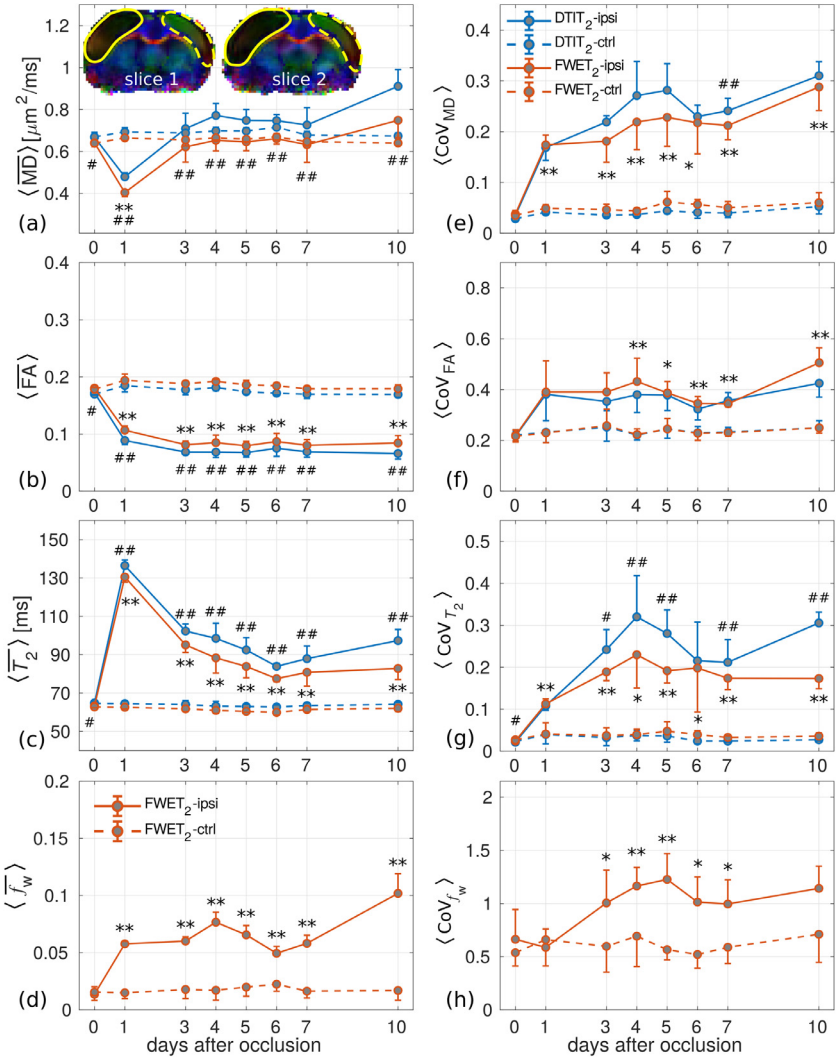

Fig. 4. (a–d) Temporal evolution of the mean, ⟨…⟩, of $DTIT_2$ (blue lines) and $FWET_2$ (red lines) parameters for the ipsilateral (solid lines) and contralateral (dashed lines) ROIs (shown overlaid to the colour-coded FA, inset in (a)), taken over 4 animals. (e–h) Temporal evolution of the mean of CoV for each parameter, taken over 4 animals. Error bars denote the SEM. $^{*},^{\#}\ p < 0.05$; $^{**},^{\#\#}\ p < 0.01$.

water fractions ($f_w \geq 0.07$) in the ipsilateral hemisphere was additionally performed. Both MD_t and $T_{2,t}$ show a negative correlation with f_w on day 1 after stroke, whereas the correlation turns positive for later time points. The slope of this correlation tends to decrease with time. When these points are mapped back, it can be seen that these voxels are located in the aforementioned inner border zone between the external capsule and the cortex. Interestingly, the outer border zone does not show the previously discussed correlation. A number of points with increased f_w values can be observed in the contralateral hemisphere, referring to voxels located at the interface between the tissue and the CSF in the ventricles (green arrows). As expected, the MD_t, FA_t and $T_{2,t}$ values for those voxels show normal values. This behaviour also holds for MD_t and FA_t in the ipsilateral hemisphere.

3.3. ROI analysis

The group-averaged, temporal change in $DTIT_2$ and $FWET_2$ parameters and CoV values for the cortex are shown in Fig. 4a–d and 4e-h, respectively. All parameters in the contralateral cortex were practically invariant compared to the ipsilateral cortex. One day after stroke, $\langle\overline{MD}\rangle$ and $\langle\overline{MD_t}\rangle$ in the ipsilateral cortex dropped by ~31% and ~39%, respectively. Beyond day 3, the values of $\langle\overline{MD}\rangle$ reached a peak on day 4 (~11%), slightly decrease until day 7 and finally increased again on day 10 (~35%). In contrast, $\langle\overline{MD_t}\rangle$ values in the ipsilateral cortex did not show significant differences compared to the contralateral cortex between days 3 and 10. At the ipsilateral cortex, $\langle\overline{MD}\rangle$ was significantly higher that $\langle\overline{MD_t}\rangle$ before ($p < 0.05$) and after stroke ($p < 0.01$). The heterogeneity analysis within the ROI (Fig. 4e) shows that $\langle CoV_{MD_t}\rangle$ in the ipsilateral cortex is significantly larger than in the contralateral side at all time points after stroke. Although $\langle CoV_{MD}\rangle$ seems visually larger than $\langle CoV_{MD_t}\rangle$ at all time points, the difference is only significant 7 days after stroke ($p < 0.01$).

Both $\langle\overline{FA}\rangle$ and $\langle\overline{FA_t}\rangle$ were significantly lower ($p < 0.01$) in the ipsilateral cortex from day 1 (~52% and ~45%, respectively) and continued to slightly decrease from day 3 through 10 (~61% and ~53%). $\langle\overline{FA}\rangle$ was significantly lower than $\langle\overline{FA_t}\rangle$ both before ($p < 0.05$) and after stroke ($p < 0.01$). It is also shown that, although $\langle CoV_{FA_t}\rangle$ at the ipsilateral cortex is visually larger than that in the contralateral cortex, the difference is only significant between days 4 and 10 (Fig. 4f).

Both $\langle\overline{T_2}\rangle$ and $\langle\overline{T_{2,t}}\rangle$ were significantly larger at the ipsilateral cortex than the contralateral cortex at all time points after stroke ($p < 0.01$). Both relaxation times peaked 1 day after stroke (~112% and 108%, respectively), started dropping until day 6 (~34% and ~30%) and rose again from day 7 until day 10 (~52% and ~33%). $\langle\overline{T_2}\rangle$ was significantly higher than $\langle\overline{T_{2,t}}\rangle$ before occlusion ($p < 0.05$) and after occlusion ($p < 0.01$). The analysis of ROI heterogeneity (Fig. 4g) shows that $\langle CoV_{T_{2,t}}\rangle$ in the ipsilateral cortex is significantly larger than in the contralateral cortex at all time points after stroke. Moreover, $\langle CoV_{T_2}\rangle$ is significantly larger than $\langle CoV_{T_{2,t}}\rangle$ at all time points, with the exception of day 6.

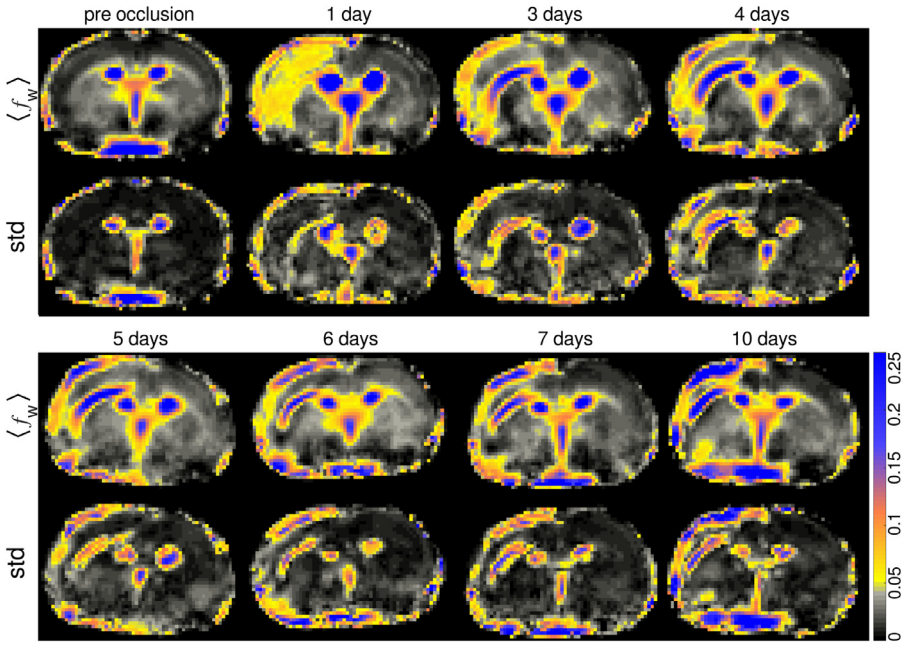

Fig. 5. Temporal evolution of the voxel-wise mean, $\langle f_w \rangle$, and standard deviation, std, maps of f_w taken over four animals.

The free water fraction (Fig. 4d) in the contralateral cortex averaged across all time points was $\langle \overline{f_w} \rangle = 0.018 \pm 0.007$. $\langle \overline{f_w} \rangle$ in the ipsilateral cortex was ~287% higher than in the contralateral cortex 1 day after stroke. The peak value was reached on day 4 (~347%), $\langle \overline{f_w} \rangle$ then starts dropping until day 6, after which it rises again with a maximum increase on day 10 (~500%). All changes were significant compared to the contralateral cortex ($p < 0.01$). The analysis of heterogeneity revealed that 1 day after stroke $\langle \mathrm{CoV}_{f_w} \rangle$ in the ipsilateral cortex (Fig. 4h) showed no significant differences compared to the contralateral values. However, between days 3 and 7, $\langle \mathrm{CoV}_{f_w} \rangle$ in the ipsilateral cortex was significantly larger than in the contralateral cortex.

3.4. Group-based template analysis

Fig. 5 shows the spatiotemporal evolution of the mean, $\langle f_w \rangle$, and standard deviation, std, free water fraction maps taken over the four animals, following registration to the group-based template, for each time point. The spatial and temporal behaviour of $\langle f_w \rangle$ is highly comparable to that of f_w for animal 1 (Fig. 2d). The std maps in the healthy tissue show rather low values for all time points. This is also the case for the ischaemic core, especially at 1 day after stroke, where the std map shows values similar to the ipsilateral cortex. Conversely, the outer and inner border zones of the ischaemic tissue tend to show more heterogeneity across animals, as demonstrated by the higher std values in Fig. 5.

3.5. Histology

Fig. 6 shows the f_w map of the lesion (red ROI, overlaid onto the FA maps) and the corresponding overview of H&E, Iba-1, and GFAP stains for the same animal and at the adjacent slice/section position (close to Bregma −0.48 mm). Note that f_w shows a very similar spatiotemporal heterogeneity (Fig. 6a), consistent with the corresponding $\langle f_w \rangle$ in Fig. 5. H&E staining (sensitive to detect non-specific cell and tissue morphology) revealed coexisting pathological changes (Fig. 6b). For immunoreactivity, Iba-1(+) for microglia/macrophages and GFAP(+) for astrocytes were used to indicate both the extent of cellular responses and the spatial relation in the ischaemic cortex at different time points (Fig. 6c and d).

In histology, three sub-regions of the ischaemic cortical lesion (Fig. 8a) were examined separately. Fig. 7 shows the high magnification images from the respective sub-region at different time points shown in Fig. 6. As seen in the representative H&E images (Fig. 7a–d), massive neuronal cell vacuoles (left-hand side inset, green arrow heads), with sizes ranging from 10 to 25 μm, and vacuoles of neuropil, also defined as spongiosis and oedema, (right-hand side inset, green arrows), with sizes ranging from 5 to 25 μm, were found in three sub-regions of the ischaemic cortex on day 1 after MCAo (Fig. 7b), as compared with the non-stroke animal (Fig. 7a). Perivascular oedema was also observed (blue arrow, Fig. 7b). On day 3 after MCAo, extensive perivascular oedema, with perivascular space diameter ranging from 50 to 200 μm, was found (blue arrows, Fig. 7c), whereas vacuolation of neuronal cell and of the neuropil was less evident. Cavitation was initially observed in the inner border zone, while cerebral subleptomeningeal oedema, denoted by the enhanced space between arachnoid and pia matter containing CSF, with thickness varying from 50 to 100 μm (black arrow) was shown in the outer border zone on day 3 (Fig. 7c). On day 10 after MCAo, massive cyst-like cavitation (asterisks, Fig. 7d), with sizes varying from 50 to 250 μm, was observed at the inner border zone, while cerebral subleptomeningeal oedema (black arrow, Fig. 7d), with thickness varying from 50 to 150 μm, was also shown in the outer border zone. Liquefactive necrosis accompanied by destroyed tissue cytoarchitecture and fluid-filled cysts (red arrows, Fig. 7d) was also found from the outer border to the core area on day 10 after stroke.

In addition to the detection of morpho-histopathological changes in the ischaemic sections, IHC staining was tested for Iba-1 and GFAP immunoreactivity in the ischaemic injury. The negative control section was tested, showing no brown DAB reaction for IHC (data not shown). For microglia/macrophages, activated amoeboid Iba-1(+) cells with a round cell body, and a small number of short processes were found in the ischaemic cortex, along with the formation of vacuoles of the neuronal cell and of the neuropil on day 1 after MCAo, as compared to inactive ramified Iba-1(+) cells of non-stroke (insets, Fig. 7e vs. 7f). On day 3 after stroke, massive activated rounded Iba-1(+) cells were found in both border zones (magenta arrows, Fig. 7g) but not in the core of the lesion, indicating the infiltration of Iba-1(+) macrophages (Fig. 7g). On day 10 after stroke, a significant accumulation of activated rounded Iba-1(+) cells (magenta arrows, Fig. 7h) was observed in the lesioned area, whereas severe liquefied necrosis was observed in the outer border zone.

For the case of astrocytes, GFAP immunoreactivity was found to be enhanced after stroke (Fig. 7i–l). On day 1 after stroke, brain tissues showed a strong immunoreactivity to reactive astrocytes with moderate

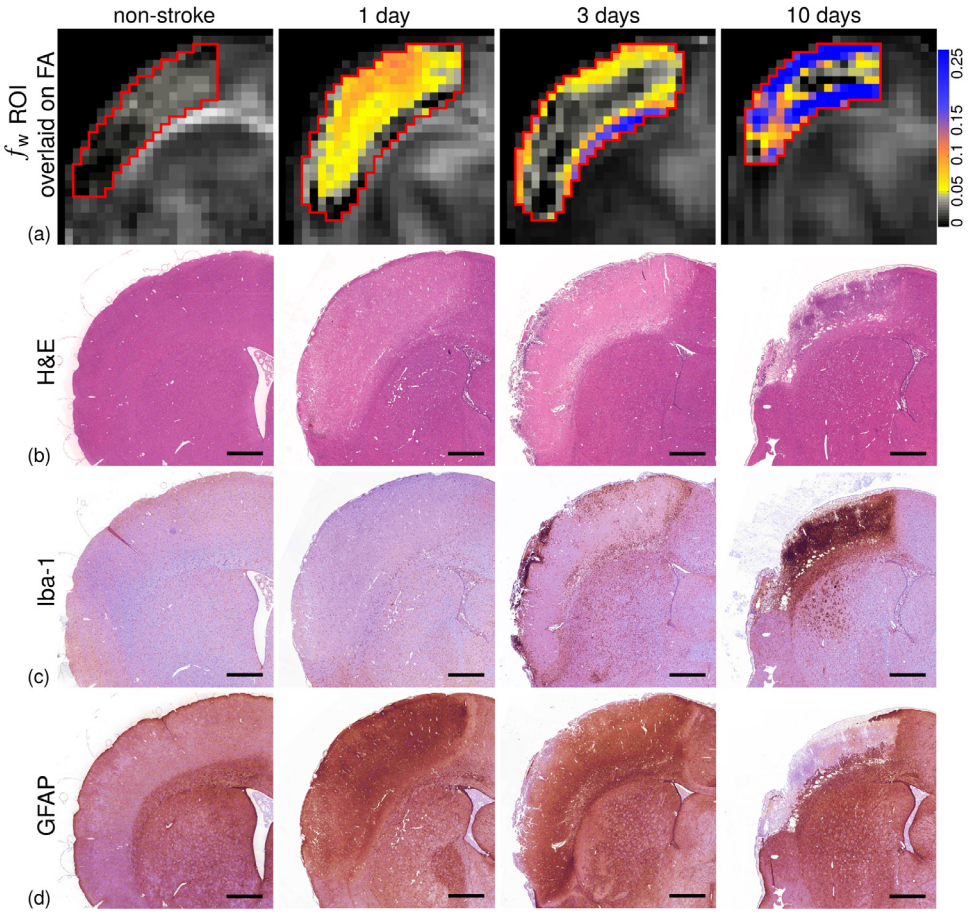

Fig. 6. (a) Spatiotemporal evolution of the f_w maps at the cortical lesion (delineated by the red ROI overlaid onto FA maps) and (b–d) corresponding overview of the histological staining. The maps of f_w show the lesion heterogeneity over time (a) and the link to the histopathological changes detected with H&E (b). For IHC, Iba-1(+) stains show the infiltration and then the accumulation of microglia/macrophages (c, also see Fig. 7g and h). GFAP(+) stains show reactive astrocyte swelling prior to Iba-1(+) cell infiltration and markedly infiltrated reactive astrocytes with prominent processes surrounding the large empty cyst-like cavitation at the inner border zone in the late subacute phase (d, also see Fig. 7j and l). Note that cell immunoreactivity was detected by chromogen DAB (brown), and hematoxylin (purple) was used as nuclear counterstaining. Scale bars represent 1 mm.

cell body and process enlargement (inset, Fig. 7j) in all sub-regions of the ischaemic cortex accompanied with vacuoles in the neuronal cell and neuropil, compared to the resting astrocytes (inset, Fig. 7i) from the non-stroke animal. On day 3 after stroke, relatively few reactive astrocytes with severe cell body enlargement and a significant reduction in processes (inset, Fig. 7k) were observed in the core area whereas strongly enhanced, reactive astrocytes with prominent processes were initially observed in the inner border zone (Fig. 7k). On day 10 after stroke, the ischaemic cortex showed almost no GFAP(+) astrocytes in the core and outer border zone (Fig. 7l), whereas the inner border zone contained abundant, reactive GFAP(+) astrocytes, which appeared to be enlarged and with prominent processes (inset, Fig. 7l). In addition, the empty cyst-like cavitation (asterisks, Fig. 7l), with no counterstained nuclei (purple) inside, in the inner border zone was found to be surrounded by end-feet of reactive GFAP(+) astrocytes (yellow arrow, Fig. 7l).

3.6. *Histopathological examination and comparison with* f_w

A comparison of the spatiotemporal evolution of f_w with the semi-quantitative histopathological scoring was performed. Given the observed f_w heterogeneity at the ischaemic lesion, in order to explore the histopathological correspondence with f_w, we divided the cortical lesion into three sub-regions based on its distance to the cortical surface (Fig. 8a). Fig. 8b shows that $\langle\overline{f_w}\rangle$ (i.e. f_w averaged within the ROI and then over three animals) at the core of the lesion significantly increased on day 1 after MCAo (*, $p < 0.05$), it tended to normalise to the baseline value on day 3 and then kept increasing on day 10. At the inner border zone, $\langle\overline{f_w}\rangle$ showed a significant increase on day 3 (*, $p < 0.01$), while at the outer border zone, it significantly increased on both day 3 and day 10 (*, $p < 0.01$; #, $p < 0.05$). In particular, the ischaemic cortical lesion showed a significant f_w heterogeneity between the two adjacent sub-regions (†, ‡; $p < 0.05$), i.e. f_w reduced to baseline values at the core area whereas it increased at the border zones on day 3.

We assessed six histopathological features related to vasogenic oedema and fluid-filled structures/pathology on H&E stained images by using mean damage scores reflecting the severity of the injury. Cerebral subleptomeningeal oedema tended to enhance from day 3 at the outer border zone (Fig. 8c). In addition, liquefactive necrosis tended to be more severe at the core and outer border zone on day 10 (Fig. 8d). On the other hand, the damage level of the perivascular oedema tended to increase on day 1 and peaking on day 3 for all sub-regions (Fig. 8e). On the contrary, vacuolation of neuronal cell and of the neuropil peaked both on day 1 and progressively diminished from day 3 for all sub-regions (Fig. 8f and 8g, respectively). Finally, cavitation at the inner border zone tended to be worse from day 3 (Fig. 8h).

4. Discussion

We have demonstrated the use of $FWET_2$ for the characterisation of the spatiotemporal evolution of ischaemic tissue from the acute to the late subacute phases of MCAo stroke animal models compared to conventional DTI and T_2-relaxometry ($DTIT_2$). Furthermore, we have related the spatiotemporal evolution of several histopathological features with the corresponding free water fraction. In the following, we shall first briefly address the validity of $FWET_2$ for modelling the DW and T_2W MRI signal in rat brain tissue and the experimental setup used in this work. In the second part, we shall discuss the results obtained using $FWET_2$ and the biophysical interpretations. Finally, we consider

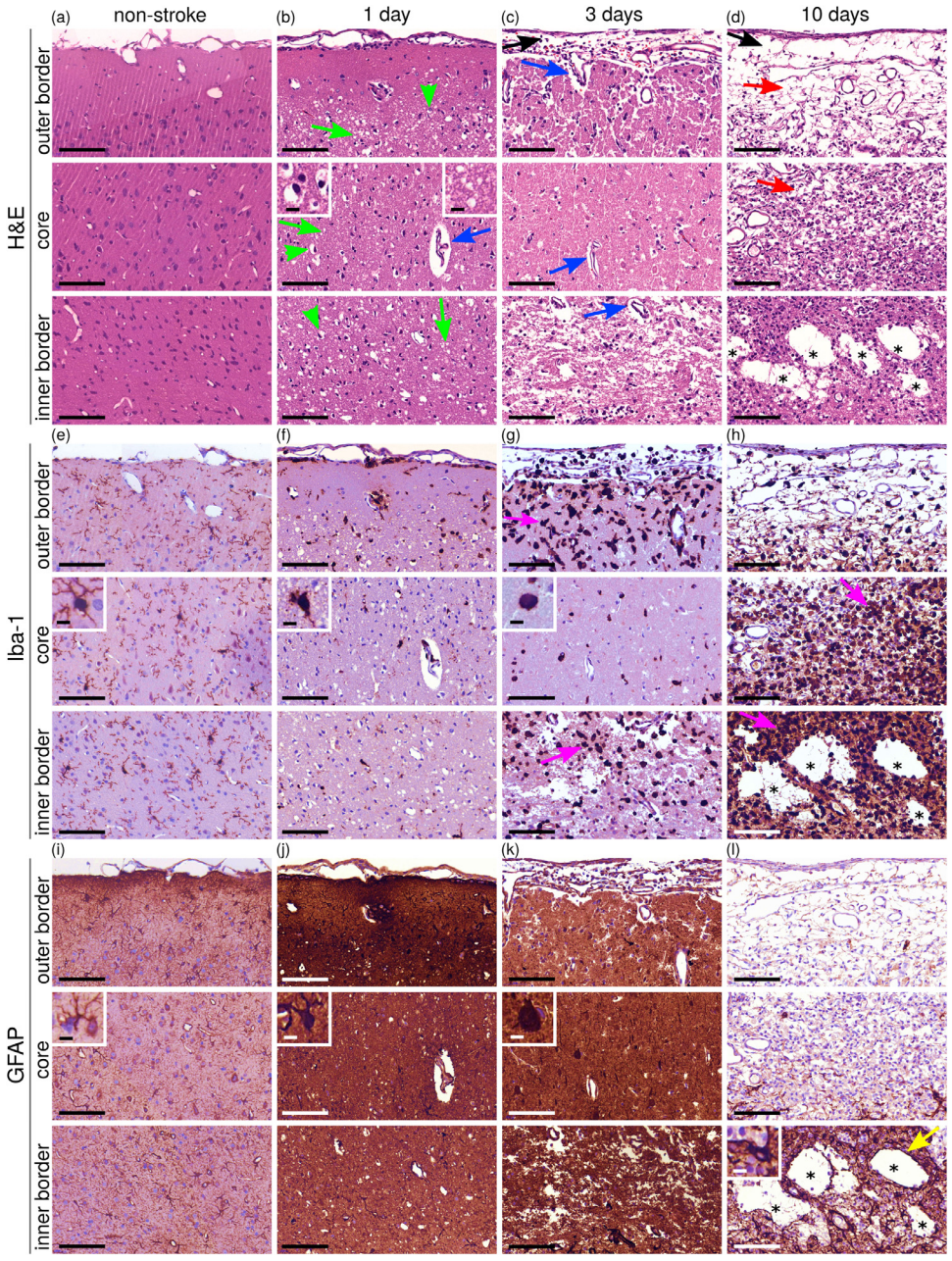

Fig. 7. Time course of the histopathological changes at the inner and outer border zones and at the core area of the cortical lesion. (a–d) H&E stains: normal tissue appearance from non-stroke (a); vacuolation of neuronal cell (left-hand side inset and green arrow heads, b) and vacuolation of the neuropil (right-hand side inset and green arrows, b) abundant in the lesion on day 1; perivascular oedema (blue arrows, b and c) shown on day 1 and increased on day 3; cavitative lesion at the inner border zone (c) shown on day 3 and empty cystic-like cavitative structures (asterisks, d) shown on day 10; cerebral subleptomeningeal oedema (black arrows, c and d) detected on day 3; liquefactive necrosis (red arrows, d) particularly at the outer border zone on day 10. (e–h) Iba-1 staining: inactive, ramified Iba-1(+) microglia/macrophages with a complex network of processes for non-stroke (inset, e); activated, amoeboid Iba-1(+) cells with a round cell body, and relatively few and short processes shown on day 1 (inset, f); activated, rounded Iba-1(+) cells with no processes (inset, g) and infiltrated into both border zones on day 3 (magenta arrows, g) and accumulated in the lesion on day 10 (magenta arrows, h). (i–l) GFAP staining: resting GFAP(+) astrocytes (inset, i) from non-stroke; reactive GFAP(+) astrocytes with moderate enlargement in cell body and processes (inset, j) on day 1; reactive GFAP(+) astrocytes with severe cell body enlargement and a significant reduction in processes (inset, k) on day 3; few enhanced GFAP(+) astrocytes with prominent processes shown at the inner border zone (adjacent to white matter) on day 3 (k); abundant reactive GFAP(+) astrocytes, which appear to be enlarged with prominent processes (inset, l) accumulated and empty cystic like cavitative structures (asterisks, l) surrounded by reactive GFAP(+) astrocytes (yellow arrow, l) on day 10. The highly magnified images are representative from Fig. 6. Scale bars represent 100 μm and 10 μm for subfigures and insets, respectively.

the prospective added value of $FWET_2$ for clinical practice and its limitations.

4.1. Experimental setup and model validation

In order to set the experimental protocol, some considerations were made partly based on the work by Collier et al. (2017). Collier et al. showed that, for similar biological conditions, the elements of the Cramér-Rao lower-bound (CRLB) matrix of the $FWET_2$ estimation problem are significantly reduced in the range TE ~ 70–120 ms, but tend to decrease asymptotically for TE greater than 130 ms. In contrast, increasing TE leads to a reduction of the SNR values, especially for DW images (Fig 1a). Thus, since an exhaustive optimisation of the experimental protocol for $FWET_2$ was beyond the scope of this work, a maximum TE of 130 ms was used as a compromise between a sufficient reduction of the CRLB matrix elements and high enough SNR values.

In terms of the validity of the $FWET_2$ model, we have demonstrated that $FWET_2$ has lower residual values, and this is particularly evident at lower *b*-values. This is in agreement with the fact that the signal in free water attenuates more quickly with increasing *b*-values than in tissue, and therefore lower *b*-values are more sensitive to faster diffusing molecules. Furthermore, with the exception of some voxels randomly distributed over the slice, the AIC analysis showed that $FWET_2$ could describe the data statistically better than $DTIT_2$ for most parts of the brain, where the SNR values are above ~5. That is to say, the brain parenchyma is indeed likely to contain a free water compartment. For low SNR voxels, the multi-compartment nature of $FWET_2$ makes the parameter estimation problem prone to instabilities (Bergmann et al., 2020; Hoy et al., 2014; Jelescu et al., 2016). Conversely, the $DTIT_2$ estimation problem can be linearised, and, therefore, its parameters of interest can be robustly estimated, even at low SNR values, using a weighted linear minimisation (Eq. (3)) (Veraart et al., 2013). Consequently, AIC

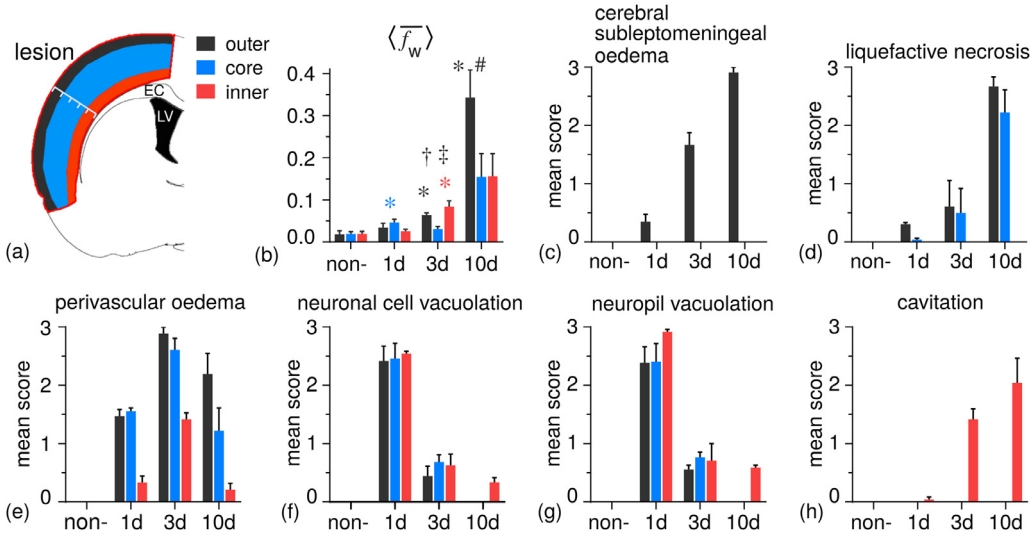

Fig. 8. Temporal evolution of $\langle \overline{f_w} \rangle$ related to tissue histopathological damage scores. Three examined sub-regions of the ischaemic cortical lesion were delineated by their distance to the cortical surface (a). An increase of $\langle \overline{f_w} \rangle$ at the outer border zone (b) mainly relates to the increase of cerebral subleptomeningeal oedema (c) and liquefactive necrosis (d) with time, whereas the increased $\langle \overline{f_w} \rangle$ at the inner border zone (b) matches the temporal changes of the cavitation damage level (h). On the contrary, the temporal change of $\langle \overline{f_w} \rangle$ at the core was affected by multiple histopathological features, including liquefactive necrosis (d), perivascular oedema (e), and neuronal cell and neuropil vacuolation (f and g, respectively). Error bars denote SEM. EC, external capsule; LV, lateral ventricle; d, day(s) after occlusion; non-, non-stroke. Symbols definition: *, significantly different from non-; #, significantly different from 1d; †, significant difference between outer and core; ‡, significant difference between inner and core.

values in very low SNR regions (far from the receive coil) must be considered cautiously.

4.2. Spatiotemporal evolution of $DTIT_2$ vs $FWET_2$ parameters

$FWET_2$ assumes that the DW and T_2W MRI signal is generated from two compartments, namely free fluid (of relative size f_w) and tissue. The presence of a fraction, f_w, of free fluid within the voxel of interest induces a positive bias in the conventional mean diffusivity, MD, and transverse relaxation time, T_2, compared to the tissue-specific counterparts, MD_t and $T_{2,t}$. The larger the f_w, the larger the bias. The maps in Fig. 2 demonstrate that MD_t and $T_{2,t}$ have a temporal evolution qualitatively comparable to their conventional counterparts, yet the conditions $MD \geq MD_t$ and $T_2 \geq T_{2,t}$ were encountered at all times, which is in agreement with the presence of a free water compartment. However, the heterogeneity analysis of the corresponding maps (Fig. 4e-h) revealed that MD_t and $T_{2,t}$ in the cortex were more homogeneous than the conventional counterpart. This suggests that the previously observed heterogeneity in the conventional MD and T_2 (Asato et al., 1991; S. P. Lin et al., 2002; T. N. Lin et al., 2002; Wegener et al., 2006) can, in part, be accounted for by the presence of the heterogeneously distributed free water fraction.

4.3. Biophysical interpretation

We demonstrated that $FWET_2$ parameters (in particular f_w) offer valuable information for the biophysical characterisation of ischaemic tissue using MRI. In the early acute stage (~1 day), f_w was shown to homogeneously increase in the whole ischaemic area (Figs. 2d, 4d,h and 5). In turn, this increment resulted in a slight reduction of MD_t and $T_{2,t}$ compared to their conventional counterparts (Figs. 2a,c and 4a,c), yet MD_t and $T_{2,t}$ differed from the contralateral values. The latter is in line with the current understanding of the biophysical processes occurring in this phase of stroke, namely cellular swelling (Knight et al., 1991) and neurite beading (Budde and Frank, 2010) as a consequence of the extended cytotoxic oedema (decrease in MD_t) and the increase in the total water content (increase in $T_{2,t}$) as a consequence of vasogenic oedema, which initially coexists with cytotoxic oedema (Kamman et al., 1988; Knight et al., 1991; T. N. Lin et al., 2002; Matsumoto et al., 1995). Our H&E histology results further demonstrate that the increase in f_w at the core during the early acute stage is mainly linked to the development of three features (Fig. 8e–g), namely (i) neuronal cell vacuolation with vacuoles sizes ranging from 10 to 25 μm, (ii) neuropil vacuolation with vacuoles sizes lying in the range 5 to 25 μm and (iii) perivascular oedema (to a lesser extend), with the perivascular sizes ranging from 50 to 200 μm (Fig. 7b). These fluid-filled compartments are generally larger than the root mean square displacement for free water in our experiments (~8 μm), leading to the increase in f_w. However, the fact that $T_{2,t}$ in the ipsilateral cortex remains larger than that in the contralateral side indicates that the increment in f_w cannot be the only explanation for the increase in conventional T_2. The GFAP immunohistochemistry taken on day 1 after stroke showed the presence of swollen astrocytes in the lesion, which typically denote intracellular swelling (Fig. 7j), thus suggesting that the remaining increase in conventional T_2 might be due to the increase in the size of the intracellular space, which is consistent with cytotoxic oedema. This also agrees with the fact that MD_t in the ipsilateral cortex was found to be lower than that in the contralateral side on day 1 after stroke.

Starting on day 3 after MCAo, $FWET_2$ maps (in particular f_w) showed a highly heterogeneous temporal evolution, which we have divided into three regions. The core region, where $FWET_2$ maps progressively approach the contralateral side values and the outer and inner border zones, where f_w increases with time (Figs. 2d and 5). This spatial organisation was found to be strikingly similar to the earlier observations for conventional MD (Hui et al., 2012; T. N. Lin et al., 2002) and T_2 (S. P. Lin et al., 2002; T. N. Lin et al., 2002; Wagner et al., 2012).

The steady normalisation of f_w at the core region starting from 3 days after stroke is in line with the observed reduction of the neuronal cell and neuropil vacuolation in the core (Fig. 8f,g). However, a peak in the perivascular oedema was seen on day 3, with a further reduction on day 10 (Fig. 8e). This implies that this mechanism might also play a role in the increase in f_w in the core area. The decrease in f_w resulted in a

reduction in the difference between MD_t and $T_{2,t}$ and their conventional counterparts. Our histopathology results show that the progressive evolution of MD_t and $T_{2,t}$ towards contralateral values at the core may be partly attributable to the development of liquefactive necrosis (Fig. 8d), which appears to be decoupled from the behaviour of f_w. Liquefactive necrosis reduces the number of barriers impeding diffusion, thereby increasing MD_t (Carano et al., 2000; Helpern et al., 1993; Jiang et al., 1997; Matsumoto et al., 1995), while also reducing $T_{2,t}$, via an increment in the amount of binding of water protons to degraded macromolecules (Wagner et al., 2012). Another mechanism observed in this work potentially leading to the normalisation of $T_{2,t}$ is the resolution of perivascular oedema (Fig. 8e), as previously suggested in the literature (S. P. Lin et al., 2002; T. N. Lin et al., 2002; Wagner et al., 2012).

The inner and outer border zones showed a different behaviour compared to the core area, starting 3 days after stroke. The inner border zone was characterised by a steady increase in f_w until day 4, a drop was observed towards day 7, and a further rise was seen on day 10 (Figs. 2 and 5). Moreover, the elevated f_w was not the only cause for the elevated conventional MD and T_2 in this area. Our histopathology results suggest that the early increase in f_w at the inner border zone (on day 3) may be dominated by the development of perivascular oedema (Fig. 8e), a less prominent contribution from neuronal cell and neuropil vacuolation (Fig. 8f,g) and, to a lesser extent, the early signs of tissue cavitation (Fig. 8h). On the other hand, the dominant factor for the later increase in f_w on day 10 appears to be the tissue cavitation and the formation of fluid-filled cysts, with typical sizes (50–250 μm) well beyond the mean water displacement in our experiments (~8 μm).

Conversely, the outer border zone was characterised by a steady increase in f_w (Figs. 2 and 5). Note that, as opposed to the inner border zone, the tissue-specific parameters MD_t and $T_{2,t}$ at the outer border zone showed similar values to those at the core. The histopathology results demonstrate that the dominant factors driving the increase in f_w were the cerebral subleptomeningeal oedema (Fig. 8c), liquefactive necrosis (Fig. 8d), perivascular oedema (Fig. 8e) and, at early stages and to a lesser extent, neuronal cell and neuropil vacuolation (Fig. 8f,g).

Having accounted for the presence of a free water compartment with characteristic D_w and $T_{2,w}$, we still observed elevated values for MD_t in the inner border zone and $T_{2,t}$ in both the inner border zone and the ischaemic core. A likely explanation for this is that the free water compartment might not be simply characterised by a single $T_{2,w}$, but rather a distribution of transverse relaxation times. This assumption is also supported by the observed positive correlation in the scatter plots of $T_{2,t}$ versus f_w seen in Fig. 3 and Table 1 (ipsi abn). A complete account for the effect of f_w on tissue-specific relaxation time should leave $T_{2,t}$ uncorrelated with f_w (e.g. the tail of points highlighted by the green arrows in Fig. 3). Besides these factors, additional mechanisms within the tissue-specific compartment could also be involved in this observation. Thus, the use of other more complex models able to account for the intra- and extra-cellular spaces (Veraart et al., 2017), in combination with the free water compartment, could further help to elucidate the biophysical mechanisms involved in the latter observations.

One of the assumptions of the $FWET_2$ model is that water exchange between compartments is negligible. An increase in the amount of exchange causes an increase in MD and a decrease in FA from conventional DTI. In the case of FWE models, the exchange is expected to induce a bias in the estimation of f_w and, therefore, in the tissue-specific diffusion tensor parameters (Pasternak et al., 2009). A similar situation would be observed in the case of the transverse relaxation time. Although water exchange has been extensively studied in the field of NMR in porous media (Eriksson et al., 2017; Kärger et al., 1988), open questions remain in relation to the exchange rate in the *in vivo* brain and its effect on the DW and T_2-relaxometry MRI metrics (Fieremans et al., 2010; Grinberg et al., 2011b; Lasič et al., 2011; Nilsson et al., 2013a, 2013b; Pasternak et al., 2009).

4.4. Clinical implications

Notwithstanding the fact that the experimental protocol used in this work impedes a direct application of $FWET_2$ in clinical practice due to its extended acquisition time, we recognise that optimisation approaches such as those based on the minimisation of the CRLB values of the parameters of interest could be utilised to reduce the acquisition time (Collier et al., 2017; Gras et al., 2017; Poot et al., 2010).

One of the most direct clinical implications of our results relates to a better understanding of the biophysical processes leading to the so-called "T_2-fogging" effect described by Asato et al. (1991) in the context of stroke assessment via conventional T_2W imaging. By means of the analysis of ROI heterogeneity (Fig. 4e–h), we showed that part of the fogging effect in T_2, i.e. the pseudo normalisation of conventional T_2 values (and also in MD) could be accounted for by the f_w maps.

Another field in which f_w is expected to add significant value is the multiparametric-based segmentation approaches of brain areas affected by stroke, such as the MRI signatures proposed by Jiang et al. (1997) or the unsupervised ISODATA (Jacobs et al., 2000). These works are based on the simultaneous use of conventional DTI and T_2-relaxometry maps (or the corresponding weighted images). It is expected that prior quantitative knowledge of the extent to which a given contrast observed in conventional metrics (or images) is due to the presence of free fluid will give valuable information for the tissue segmentation. In this regard, an intrinsic advantage of $FWET_2$ compared to conventional DTI and T_2-relaxometry methods is related to the fact that both modality-related maps lay in the same image space. Hence, the need for registration approaches between modalities is unnecessary, avoiding possible image mismatches. Given the importance of the aforementioned multiparametric tissue segmentation approaches, the added value of $FWET_2$ becomes evident.

5. Limitations

Although the use of surface coils has the advantage of delivering higher SNR values compared to volume coils, it represents a serious drawback for the estimation of the total water content (Abbas et al., 2014). This is due to the highly spatially inhomogeneous B_1 field, which has hindered the estimation of the water content in our work.

In order to reduce Gibbs-ringing artefacts, the total variation method (Perrone et al., 2015) has been used. However, although this approach has been shown to reduce the latter effect, it additionally induces unwanted smoothing of the parameter maps, and other more accurate approaches such as (Kellner et al., 2016) may be desirable for the study of ROI heterogeneity.

Another limitation of this work refers to the fact that D_w and $T_{2,w}$ are fixed using literature values. Although the values of D_w and $T_{2,w}$ are relatively well documented, there are numerous factors that can alter their values, e.g. body temperature, the concentration of proteins and other macromolecules, etc. Thus, an ideal experimental design should include the possibility of evaluating D_w and $T_{2,w}$ from the experimental data, either by placing a ROI where only free fluid is expected or by using higher T_E values, where only the signal from free fluid survives. In line with this, another limitation is the assignment of D_w and $T_{2,w}$ to the same physical compartment. Given that transverse relaxation time is sensitive to the accumulation of proteins and other macromolecules, the assumption made in this work might be an oversimplification.

6. Conclusions

We assessed the benefits and limitations of using the $FWET_2$ model for the investigation of the spatiotemporal evolution of ischaemic stroke in the MCAo stroke rat model from the acute to the late subacute phases. Parallel to the tissue-specific mean diffusivity, fractional anisotropy and

transverse relaxation time, we considered the behaviour of the conventional counterparts provided by DTI and T_2-relaxometry. The different biophysical mechanisms discussed in the literature were discussed within the framework of the $FWET_2$ model, using the histopathology results as supporting information.

We demonstrated that the quantification of the free water fraction using $FWET_2$ enables the extent of the observed changes in conventional metrics due to the presence of free water in the ischaemic tissue to be determined. We showed that the early increase in conventional T_2 normally attributed to vasogenic oedema within the ischaemic area can be partially accounted for by an increment in the fraction of free water, f_w. Furthermore, the normalisation of conventional MD and T_2 at the ischaemic core, demonstrated by other works to be due to the resolution of brain oedema and the increased of non-bound water, supports the normalisation of f_w seen in our work. Finally, the later increase in conventional MD and T_2 in the inner and outer border zones between the ischaemic core, previously demonstrated to be due to the formation of fluid-filled cysts, converges with our observation that f_w was highly elevated in these regions. That is to say, we demonstrated that f_w is initially sensitive to the pathological changes linked to the evolution of vasogenic oedema in the ischaemic core, whereas in the late subacute phase, f_w can reflect the presence of fluid-filled cysts.

Declaration of Competing Interest

None

Credit authorship contribution statement

Ezequiel Farrher: Conceptualization, Methodology, Software, Validation, Formal analysis, Investigation, Writing – original draft, Writing – review & editing, Visualization. **Chia-Wen Chiang:** Conceptualization, Methodology, Software, Validation, Formal analysis, Investigation, Writing – review & editing, Visualization. **Kuan-Hung Cho:** Conceptualization, Methodology, Software, Validation, Formal analysis, Investigation, Writing – review & editing. **Farida Grinberg:** Conceptualization, Methodology, Writing – review & editing. **Richard P. Buschbeck:** Conceptualization, Methodology, Software, Validation, Formal analysis, Investigation, Writing – review & editing. **Ming-Jye Chen:** Methodology, Validation, Formal analysis, Investigation, Writing – review & editing. **Kuo-Jen Wu:** Methodology, Validation, Formal analysis, Investigation, Resources, Writing – review & editing. **Yun Wang:** Methodology, Validation, Formal analysis, Investigation, Resources, Writing – review & editing. **Sheng-Min Huang:** Methodology, Validation, Formal analysis, Investigation, Writing – review & editing, Visualization. **Zaheer Abbas:** Methodology, Software, Formal analysis, Writing – review & editing. **Chang-Hoon Choi:** Conceptualization, Methodology, Software, Validation, Formal analysis, Investigation, Resources, Writing – review & editing, Supervision, Project administration, Funding acquisition. **N. Jon Shah:** Methodology, Resources, Writing – review & editing, Supervision, Project administration, Funding acquisition. **Li-Wei Kuo:** Conceptualization, Methodology, Software, Validation, Formal analysis, Investigation, Resources, Writing – review & editing, Supervision, Project administration, Funding acquisition.

Acknowledgements

EF thanks Dr Patricia Pais for useful discussions. We thank Ms Claire Rick for proof-reading the manuscript. This work was supported by the Ministry of Science and Technology, Taiwan [MOST-110-2927-I-400-501, MOST-110-2314-B-400-051 and MOST-109-2221-E-400-001-MY2], and the National Health Research Institutes, Miaoli, Taiwan [NHRI-BN-110-PP-06].

References

Abbas, Z., Gras, V., Möllenhoff, K., Keil, F., Oros-Peusquens, A.M., Shah, N.J., 2014. Analysis of proton-density bias corrections based on T1 measurement for robust quantification of water content in the brain at 3 Tesla. Magn. Reson. Med. 72, 1735–1745. doi:10.1002/mrm.25086.

Aja-Fernández, S., Tristán-Vega, A., Alberola-López, C., 2009. Noise estimation in single- and multiple-coil magnetic resonance data based on statistical models. Magn. Reson. Imaging 27, 1397–1409. doi:10.1016/j.mri.2009.05.025.

Albi, A., Pasternak, O., Minati, L., Marizzoni, M., Bartrés-Faz, D., Bargalló, N., Bosch, B., Rossini, P.M., Marra, C., Müller, B., Fiedler, U., Wiltfang, J., Roccatagliata, L., Picco, A., Nobili, F.M., Blin, O., Sein, J., Ranjeva, J.P., Didic, M., Bombois, S., Lopes, R., Bordet, R., Gros-Dagnac, H., Payoux, P., Zoccatelli, G., Alessandrini, F., Beltramello, A., Ferretti, A., Caulo, M., Aiello, M., Cavaliere, C., Soricelli, A., Parnetti, L., Tarducci, R., Floridi, P., Tsolaki, M., Constantinidis, M., Drevelegas, A., Frisoni, G., Jovicich, J., Consortium, T.P., 2017. Free water elimination improves test–retest reproducibility of diffusion tensor imaging indices in the brain: a longitudinal multisite study of healthy elderly subjects. Hum. Brain Mapp. 38, 12–26. doi:10.1002/hbm.23350.

Alexander, A.L., Hasan, K.M., Lazar, M., Tsuruda, J.S., Parker, D.L., 2001. Analysis of partial volume effects in diffusion-tensor MRI. Magn. Reson. Med. 45, 770–780. doi:10.1002/mrm.1105.

Andersson, J.L.R., Skare, S., Ashburner, J., 2003. How to correct susceptibility distortions in spin-echo echo-planar images: application to diffusion tensor imaging. Neuroimage 20, 870–888. doi:10.1016/S1053-8119(03)00336-7.

Arkesteijn, G.A.M., Poot, D.H.J., de Groot, M., Ikram, M.A., Niessen, W.J., van Vliet, L.J., Vernooij, M.W., Vos, F.M., 2017. CSF contamination-invariant statistics in conventional diffusion-weighted MRI of the fornix. Biomed. Phys. Eng. Express 3 (6), 65003. doi:10.1088/2057-1976/aa890e.

Asato, R., Okumura, R., Konishi, J.J., 1991. Fogging effect in mr of cerebral infarct. J. Comput. Assist. Tomogr. 15, 160–162. doi:10.1097/00004728-199101000-00029.

Avants, B.B., Tustison, N.J., Song, G., Cook, P.A., Klein, A., Gee, J.C., 2011. A reproducible evaluation of ANTs similarity metric performance in brain image registration. Neuroimage 54, 2033–2044. doi:10.1016/j.neuroimage.2010.09.025.

Basser, P.J., Pierpaoli, C., 1996. Microstructural and physiological features of tissues elucidated by quantitative-diffusion-tensor MRI. J. Magn. Reson. B 111, 209–219. doi:10.1006/jmrb.1996.0086.

Bergmann, Ø., Henriques, R., Westin, C.F., Pasternak, O., 2020. Fast and accurate initialization of the free-water imaging model parameters from multi-shell diffusion MRI. NMR Biomed. 33, e42. doi:10.1002/nbm.4219.

Bernin, D., Topgaard, D., 2013. NMR diffusion and relaxation correlation methods: new insights in heterogeneous materials. Curr. Opin. Colloid Interface Sci. 18, 166–172. doi:10.1016/j.cocis.2013.03.007.

Bihan, D.Le, 2007. The “wet mind”: water and functional neuroimaging. Phys. Med. Biol. 52, R57. doi:10.1088/0031-9155/52/7/R02.

Budde, M.D., Frank, J.A., 2010. Neurite beading is sufficient to decrease the apparent diffusion coefficient after ischemic stroke. Proc. Natl. Acad. Sci. U. S. A. 107, 14472–14477. doi:10.1073/pnas.1004841107.

Burnham, K.P., Anderson, D.R., 1998. Information theory and log-likelihood models: a basis for model selection and inference. In: Model Selection and Inference. Springer, New York, NY, pp. 49–97. doi:10.1007/978-1-4757-2917-7_2.

Carano, R.A.D., Li, F., Irie, K., Helmer, K.G., Silva, M.D., Fisher, M., Sotak, C.H., 2000. Multispectral analysis of the temporal evolution of cerebral ischemia in the rat brain. J. Magn. Reson. Imaging 12, 842–858 10.1002/1522-2586(200012)12:6-842::AID-JMRI-73.0.CO;2-5.

Chen, S.T., Hsu, C.Y., Hogan, E.L., Maricq, H., Balentine, J.D., 1986. A model of focal ischemic stroke in the rat: reproducible extensive cortical infarction. Stroke 17, 738–743. doi:10.1161/01.STR.17.4.738.

Cho, K.H., Huang, S.M., Choi, C.H., Chen, M.J., Chiang, H.H., Buschbeck, R.P., Farrher, E., Jon Shah, N., Garipov, R., Chang, C.P., Chang, H., Kuo, L.W., 2019. Development, integration and use of an ultrahigh-strength gradient system on a human-size 3 T magnet for small animal MRI. PLoS ONE 14, e0217916. doi:10.1371/journal.pone.0217916.

Collier, Q., Veraart, J., den Dekker, A.J., Vanhevel, F., Parizel, P.M., Sijbers, J., 2017. Solving the free water elimination estimation problem by incorporating T2 relaxation properties. In: Proc. Int. Soc. Magn. Reson. Med. 25, p. 1783.

Eriksson, S., Elbing, K., Söderman, O., Lindkvist-Petersson, K., Topgaard, D., Lasič, S., 2017. NMR quantification of diffusional exchange in cell suspensions with relaxation rate differences between intra and extracellular compartments. PLoS ONE 12, e0177273. doi:10.1371/journal.pone.0177273.

Farrher, E., Grinberg, F., Kuo, L.W., Cho, K.H., Buschbeck, R.P., Chen, M.J., Chiang, H.H., Choi, C.H., Shah, N.J., 2020. Dedicated diffusion phantoms for the investigation of free water elimination and mapping: insights into the influence of T2 relaxation properties. NMR Biomed. 33, e4210. doi:10.1002/nbm.4210.

Fieremans, E., Novikov, D.S., Jensen, J.H., Helpern, J.A., 2010. Monte Carlo study of a two-compartment exchange model of diffusion. NMR Biomed. 23, 711–724. doi:10.1002/nbm.1577.

Gras, V., Farrher, E., Grinberg, F., Shah, N.J., 2017. Diffusion-weighted DESS protocol optimization for simultaneous mapping of the mean diffusivity, proton density and relaxation times at 3 Tesla. Magn. Reson. Med. 78. doi:10.1002/mrm.26353.

Grinberg, F., Ciobanu, L., Farrher, E., Shah, N.J., 2012. Diffusion kurtosis imaging and log-normal distribution function imaging enhance the visualisation of lesions in animal stroke models. NMR Biomed. 25. doi:10.1002/nbm.2802.

Grinberg, F., Farrher, E., Ciobanu, L., Geffroy, F., Le Bihan, D., Shah, N.J., 2014. Non-Gaussian diffusion imaging for enhanced contrast of brain tissue affected by ischemic stroke. PLoS ONE 9. doi:10.1371/journal.pone.0089225.

Grinberg, F., Farrher, E., Kaffanke, J., Oros-Peusquens, A.M., Shah, N.J., 2011a. Non-Gaussian diffusion in human brain tissue at high b-factors as examined by a combined diffusion kurtosis and biexponential diffusion tensor analysis. Neuroimage 57. doi:10.1016/j.neuroimage.2011.04.050.

Grinberg, F., Farrher, E., Oros-Peusquens, A.M., Shah, N.J., 2011b. Random walks in model brain tissue. AIP Conf. Proc. 1330, 31–34. doi:10.1063/1.3562226.

Gudbjartsson, H., Patz, S., 1995. The Rician distribution of noisy MRI data. Magn. Reson. Med. 34, 910–914. doi:10.1002/mrm.1910340618.

Helpern, J.A., Dereski, M.O., Knight, R.A., Ordidge, R.J., Chopp, M., Qing, Z.X., 1993. Histopathological correlations of nuclear magnetic resonance imaging parameters in experimental cerebral ischemia. Magn. Reson. Imaging 11, 241–246. doi:10.1016/0730-725X(93)90028-C.

Hoehn, M., Nicolay, K., Franke, C., Van Sanden, B.Der, 2001. Application of magnetic resonance to animal models of cerebral Ischemia. J. Magn. Reson. Imaging 14, 491–509. doi:10.1002/jmri.1213.

Hoy, A.R., Kecskemeti, S.R., Alexander, A.L., 2015. Free water elimination diffusion tractography: a comparison with conventional and fluid-attenuated inversion recovery, diffusion tensor imaging acquisitions. J. Magn. Reson. Imaging 42, 1572–1581. doi:10.1002/jmri.24925.

Hoy, A.R., Koay, C.G., Kecskemeti, S.R., Alexander, A.L., 2014. Optimization of a free water elimination two-compartment model for diffusion tensor imaging. Neuroimage 103, 323–333. doi:10.1016/j.neuroimage.2014.09.053.

Hoy, A.R., Ly, M., Carlsson, C.M., Okonkwo, O.C., Zetterberg, H., Blennow, K., Sager, M.A., Asthana, S., Johnson, S.C., Alexander, A.L., Bendlin, B.B., 2017. Microstructural white matter alterations in preclinical Alzheimer's disease detected using free water elimination diffusion tensor imaging. PLoS ONE 12, 1–21. doi:10.1371/journal.pone.0173982.

Hui, E.S., Du, F., Huang, S., Shen, Q., Duong, T.Q., 2012. Spatiotemporal dynamics of diffusional kurtosis, mean diffusivity and perfusion changes in experimental stroke. Brain Res. 1451, 100–109. doi:10.1016/j.brainres.2012.02.044.

Jacobs, M.A., Knight, R.A., Soltanian-Zadeh, H., Zheng, Z.G., Goussev, A.V., Peck, D.J., Windham, J.P., Chopp, M., 2000. Unsupervised segmentation of multiparameter MRI in experimental cerebral ischemia with comparison to T2, diffusion, and ADC MRI parameters and histopathological validation. J. Magn. Reson. Imaging 11, 425–437 10.1002/(SICI)1522-2586(200004)11:4<425::AID–JMRI11>3.0.CO;2-0.

Jelescu, I.O., Veraart, J., Fieremans, E., Novikov, D.S., 2016. Degeneracy in model parameter estimation for multi-compartmental diffusion in neuronal tissue. NMR Biomed. 29, 33–47. doi:10.1002/nbm.3450.

Jensen, J.H., Falangola, M.F., Hu, C., Tabesh, A., Rapalino, O., Lo, C., Helpern, J.A., 2011. Preliminary observations of increased diffusional kurtosis in human brain following recent cerebral infarction. NMR Biomed. 24, 452–457. doi:10.1002/nbm.1610.

Jiang, Q., Chopp, M., Zhang, Z.G., Knight, R.A., Jacobs, M., Windham, J.P., Peck, D., Ewing, J.R., Welch, K.M.A., 1997. The temporal evolution of MRI tissue signatures after transient middle cerebral artery occlusion in rat. J. Neurol. Sci. 145, 15–23. doi:10.1016/S0022-510X(96)00286-9.

Jiang, Q., Zhang, Z.G., Chopp, M., Helpern, J.A., Ordidge, R.J., Garcia, J.H., Marchese, B.A., Qing, Z.X., Knight, R.A., 1993. Temporal evolution and spatial distribution of the diffusion constant of water in rat brain after transient middle cerebral artery occlusion. J. Neurol. Sci. 120, 123–130. doi:10.1016/0022-510X(93)90262-W.

Kamman, R.L., Go, K.G., Brouwer, W., Berendsen, H.J.C., 1988. Nuclear magnetic resonance relaxation in experimental brain edema: effects of water concentration, protein concentration, and temperature. Magn. Reson. Med. 6, 265–274. doi:10.1002/mrm.1910060304.

Kärger, J., Pfeifer, H., Heink, W., 1988. Principles and applications of self-diffusion measurements by nuclear magnetic resonance. In: Waugh, J. (Ed.), Advances in Magnetic Resonance. Academic Press, Inc., pp. 1–89 1250 Sixth Avenue San Diego, California 92101.

Kellner, E., Dhital, B., Kiselev, V.G., Reisert, M., 2016. Gibbs-ringing artifact removal based on local subvoxel-shifts. Magn. Reson. Med. 76 (5), 1574–1581. doi:10.1002/mrm.26054.

Knight, R.A., Dereski, M.O., Helpern, J.A., Ordidge, R.J., Chopp, M., 1994. Magnetic resonance imaging assessment of evolving focal cerebral ischemia: comparison with histopathology in rats. Stroke 25, 1252–1261. doi:10.1161/01.STR.25.6.1252.

Knight, R.A., Ordidge, R.J., Helpern, J.A., Chopp, M., Rodolosi, L.C., Peck, D., 1991. Temporal evolution of ischemic damage in rat brain measured by proton nuclear magnetic resonance imaging. Stroke 22, 802–808. doi:10.1161/01.STR.22.6.802.

Lasič, S., Nilsson, M., Lätt, J., Ståhlberg, F., Topgaard, D., 2011. Apparent exchange rate mapping with diffusion MRI. Magn. Reson. Med. 66, 356–365. doi:10.1002/mrm.22782.

Lätt, J., Nilsson, M., van Western, D., Wirestam, R., Ståhlberg, F., Brockstedt, S., 2009. Diffusion-weighted MRI measurements on stroke patients reveal water-exchange mechanisms in sub-acute ischaemic lesions. NMR Biomed. 22, 619–628. doi:10.1002/nbm.1376.

Leemans, A., Jeurissen, B., Sijbers, J., Jones, D.K., 2009. ExploreDTI: a graphical toolbox for processing, analizing and visualizing diffusion MR data. In: Proc. Int. Soc. Magn. Reson. Med. 17, 3537.

Lin, S.P., Schmidt, R.E., McKinstry, R.C., Ackerman, J.J., Neil, J.J., 2002. Investigation of mechanisms underlying transient T2 normalization in longitudinal studies of ischemic stroke. J. Magn. Reson. Imaging 15, 130–136. doi:10.1002/jmri.10052.

Lin, T.N., Sun, S.W., Cheung, W.M., Li, F., Chang, C., 2002. Dynamic changes in cerebral blood flow and angiogenesis after transient focal cerebral ischemia in rats: evaluation with serial magnetic resonance imaging. Stroke 33, 2985–2991. doi:10.1161/01.STR.0000037675.97888.9D.

Liu, H.S., Shen, H., Harvey, B.K., Castillo, P., Lu, H., Yang, Y., Wang, Y., 2011. Post-treatment with amphetamine enhances reinnervation of the ipsilateral side cortex in stroke rats. Neuroimage 56, 280–289. doi:10.1016/j.neuroimage.2011.02.049.

Maier-Hein, K.H., Westin, C.F., Shenton, M.E., Weiner, M.W., Raj, A., Thomann, P., Kikinis, R., Stieltjes, B., Pasternak, O., 2015. Widespread white matter degeneration preceding the onset of dementia. Alzheimer's Dement. 11, 485–493. doi:10.1016/j.jalz.2014.04.518, e2.

Manjón, J.V., Coupé, P., Martí-Bonmatí, L., Collins, D.L., Robles, M., 2010. Adaptive non-local means denoising of MR images with spatially varying noise levels. J. Magn. Reson. Imaging 31, 192–203. doi:10.1002/jmri.22003.

Matsumoto, K., Lo, E.H., Pierce, A.R., Wei, H., Garrido, L., Kowall, N.W., 1995. Role of vasogenic edema and tissue cavitation in ischemic evolution on diffusion-weighted imaging: comparison with multiparameter MR and immunohistochemistry. Am. J. Neuroradiol. 16, 1107–1115.

Metzler-Baddeley, C., O'Sullivan, M.J., Bells, S., Pasternak, O., Jones, D.K., 2012. How and how not to correct for CSF-contamination in diffusion MRI. Neuroimage 59, 1394–1403. doi:10.1016/j.neuroimage.2011.08.043.

Molina-Romero, M., Gómez, P.A., Sperl, J.I., Czisch, M., Sämann, P.G., Jones, D.K., Menzel, M.I., Menze, B.H., 2018. A diffusion model-free framework with echo time dependence for free-water elimination and brain tissue microstructure characterization. Magn. Reson. Med. 80, 2155–2172. doi:10.1002/mrm.27181.

Moseley, M.E., Cohen, Y., Mintorovitch, J., Chileuitt, L., Shimizu, H., Kucharczyk, J., Wendland, M.F., Weinstein, P.R., 1990. Early detection of regional cerebral ischemia in cats: comparison of diffusion- and T2-weighted MRI and spectroscopy. Magn. Reson. Med. 14, 330–346. doi:10.1002/mrm.1910140218.

Nilsson, M., Lätt, J., Van Westen, D., Brockstedt, S., Lasič, S., Ståhlberg, F., Topgaard, D., 2013a. Noninvasive mapping of water diffusional exchange in the human brain using filter-exchange imaging. Magn. Reson. Med. 69, 1572–1580. doi:10.1002/mrm.24395.

Nilsson, M., Van Westen, D., Ståhlberg, F., Sundgren, P.C., Lätt, J., 2013b. The role of tissue microstructure and water exchange in biophysical modelling of diffusion in white matter. Magn. Reson. Mater. Phys. Biol. Med. 26, 345–370. doi:10.1007/s10334-013-0371-x.

Ofori, E., Pasternak, O., Planetta, P.J., Li, H., Burciu, R.G., Snyder, A.F., Lai, S., Okun, M.S., Vaillancourt, D.E., 2015. Longitudinal changes in free-water within the substantia nigra of Parkinson's disease. Brain 138, 2322–2331. doi:10.1093/brain/awv136.

Ordidge, R.J., Helpern, J.A., Knight, R.A., Qing, Z., Welch, K.M.A., 1991. Investigation of cerebral ischemia using magnetization transfer contrast (MTC) MR imaging. Magn. Reson. Imaging 9, 895–902. doi:10.1016/0730-725X(91)90533-R.

Pasternak, O., Sochen, N., Gur, Y., Intrator, N., Assaf, Y., 2009. Free water elimination and mapping from diffusion MRI. Magn. Reson. Med. 62, 717–730. doi:10.1002/mrm.22055.

Paxinos, G., Watson, C., 2004. The rat brain in stereotaxic coordinates. 5th edition, 5th ed. J. Chem. Inf. Model. doi:10.1017/CBO9781107415324.004.

Perrone, D., Aelterman, J., Pižurica, A., Jeurissen, B., Philips, W., Leemans, A., 2015. The effect of Gibbs ringing artifacts on measures derived from diffusion MRI. Neuroimage 120, 441–455. doi:10.1016/j.neuroimage.2015.06.068.

Piechnik, S.K., Evans, J., Bary, L.H., Wise, R.G., Jezzard, P., 2009. Functional changes in CSF volume estimated using measurement of water T2 relaxation. Magn. Reson. Med. 61, 579–586. doi:10.1002/mrm.21897.

Pierpaoli, C., Basser, P.J., 1996. Toward a quantitative assessment of diffusion anisotropy. Magn. Reson. Med. 36, 893–906. doi:10.1002/mrm.1910360612.

Pierpaoli, C., Jones, D.K., 2004. Removing CSF contamination in brain DT-MRIs by using a two-compartment tensor model. In: Proc. Int. Soc. Mag. Res. Med. 12, p. 1215.

Pierpaoli, C., Righini, A., Linfante, I., Tao-Cheng, J.H., Alger, J.R., Di Chiro, G., 1993. Histopathologic correlates of abnormal water diffusion in cerebral ischemia: diffusion-weighted MR imaging and light and electron microscopic study. Radiology 189, 439–448. doi:10.1148/radiology.189.2.8210373.

Planetta, P.J., Ofori, E., Pasternak, O., Burciu, R.G., Shukla, P., DeSimone, J.C., Okun, M.S., McFarland, N.R., Vaillancourt, D.E., 2016. Free-water imaging in Parkinson's disease and atypical parkinsonism. Brain 139, 495–508. doi:10.1093/brain/awv361.

Poot, D.H.J., den Dekker, A.J., Achten, E., Verhoye, M., Sijbers, J., 2010. Optimal experimental design for diffusion kurtosis imaging. Med. Imaging IEEE Trans. doi:10.1109/TMI.2009.2037915.

Smith, S.M., Jenkinson, M., Woolrich, M.W., Beckmann, C.F., Behrens, T.E.J., Johansen-Berg, H., Bannister, P.R., De Luca, M., Drobnjak, I., Flitney, D.E., Niazy, R.K., Saunders, J., Vickers, J., Zhang, Y., De Stefano, N., Brady, J.M., Matthews, P.M., 2004. Advances in functional and structural MR image analysis and implementation as FSL. Neuroimage 23, S208–S219. doi:10.1016/j.neuroimage.2004.07.051, Supple.

Sotak, C.H., 2002. The role of diffusion tensor imaging in the evaluation of ischemic brain injury - a review. NMR Biomed. 15, 561–569. doi:10.1002/nbm.786.

van Dusschoten, D., 1996. Unraveling diffusion constants in biological tissue by combining Carr-Purcell-Meiboom-Gill imaging and pulsed field gradient NMR. Magn. Reson. Med. 36, 907–913. doi:10.1002/mrm.1910360613.

van Dusschoten, D., Dejager, P.A., Vanas, H., 1995. Extracting diffusion constants from echo-time-dependent PFG NMR data using relaxation-time information. J. Magn. Reson. Ser. A 116, 22–28. doi:10.1006/jmra.1995.1185.

Van Pul, C., Jennekens, W., Nicolay, K., Kopinga, K., Wijn, P.F.F., 2005. Ischemia-induced ADC changes are larger than osmotically-induced ADC changes in a neonatal rat hippocampus model. Magn. Reson. Med. 53, 348–355. doi:10.1002/mrm.20353.

Veraart, J., Novikov, D.S., Fieremans, E., 2017. TE dependent diffusion imaging (TEdDI) distinguishes between compartmental T2 relaxation times. Neuroimage doi:10.1016/j.neuroimage.2017.09.030.

Veraart, J., Sijbers, J., Sunaert, S., Leemans, A., Jeurissen, B., 2013. Weighted linear least squares estimation of diffusion MRI parameters: strengths, limitations, and pitfalls. Neuroimage 81, 335–346. doi:10.1016/j.neuroimage.2013.05.028.

Wagner, D.C., Deten, A., Härtig, W., Boltze, J., Kranz, A., 2012. Changes in T2 relaxation time after stroke reflect clearing processes. Neuroimage 61, 780–785. doi:10.1016/j.neuroimage.2012.04.023.

Weber, R., Ramos-Cabrer, P., Hoehn, M., 2006. Present status of magnetic resonance imaging and spectroscopy in animal stroke models. J. Cereb. Blood Flow Metab. 26, 591–604. doi:10.1038/sj.jcbfm.9600241.

Wegener, S., Weber, R., Ramos-Cabrer, P., Uhlenkueken, U., Sprenger, C., Wiedermann, D., Villringer, A., Hoehn, M., 2006. Temporal profile of T2-weighted MRI distinguishes between pannecrosis and selective neuronal death after transient focal cerebral ischemia in the rat. J. Cereb. Blood Flow Metab. 26, 38–47. doi:10.1038/sj.jcbfm.9600166.

Yu, S.J., Wu, K.J., Bae, E., Wang, Y.S., Chiang, C.W., Kuo, L.W., Harvey, B.K., Greig, N.H., Wang, Y., 2020. Post-treatment with posiphen reduces endoplasmic reticulum stress and neurodegeneration in stroke brain. iScience 23, 100866. doi:10.1016/j.isci.2020.100866.